

# A HOMOGENEOUS DYNAMIC TWO-PHASE FLOW MODEL OF A VERTICAL EVAPORATOR WITH VARYING FIRING PROFILES

Axel Ohrt Johansen\*  
Added Values P/S, Lysholt Allé 10  
7100 Vejle  
Denmark

Brian Elmegaard  
Technical University of Denmark  
Department of Mechanical Engineering  
2800 Lyngby  
Denmark

## ABSTRACT

In this article we would like to demonstrate the ability to simulate the dynamic conditions in a homogeneous two-phase flow model of a power plant evaporator and thus complement the recent years, research efforts in areas related to flexibility of power production. On that basis we can contribute with new knowledge about the flow stability and dynamic effects in power plants, caused by both internal and external physical conditions, resulting in improved power plant flexibility. In this article is developed numerical model for solving a transient one dimensional compressible homogeneous two phase model, for predominantly one-dimensional flows in a vertical heated pipe element. The homogeneous model is based on the assumption of both hydraulic- and thermal equilibrium. The flow model consists of three hyperbolic fluid conservation equations; continuity, momentum and energy and the pipe wall is modelled as a one dimensional heat balance equation. The models is reformulated in the four in-dependent variables: pressure, enthalpy, velocity and wall temperature. We have implemented and tested a fifth-order WENO solver, with simplified weights functions and used it to simulate the dynamic response of evaporator tubes corresponding to SKV3, on the basis of a calibrated model, based on measurements from SKV3. The model is able to describe the entire evaporation process from sub-cooled water to super-heated steam at the outlet and verify the consequences of different firing profiles and evaporator pressure for the boiler of SKV3 .

*Keywords:* Two-phase flow, evaporator, WENO scheme, heat flux bias, dynamic response

## NOMENCLATURE

$A$	Cross-sectional flow area of pipe	$m^2$
$c$	Volume fraction of layer	—
$c_p$	Specific heat capacity (fixed p)	$kJ/kg/^\circ C$
$c_v$	Specific heat capacity (fixed v)	$kJ/kg/^\circ C$
$C$	Virtual mass force coefficient	—
$e$	Specific energy	$m^2/s^2$
$F$	Force	$N$
$f$	Shear stress (friction force)	$N/m^2$
$g$	Acceleration due to gravity	$m/s^2$
$G$	Mass flux	$kg/m^2s$

\*Corresponding author: Phone: +45 2447 9455 E-mail: [aoj@addedvalues.dk](mailto:aoj@addedvalues.dk)

$h$	Enthalpy	$\text{kJ/kg/}^{\circ}\text{C}$
$k$	Thermal conductivity	$\text{W/m/}^{\circ}\text{C}$
$l$	Length of pipe/geometry/film	$m$
$\dot{M}$	Mass flux	$\text{kg/m}^2/\text{s}$
$\dot{m}$	Mass flow rate	$\text{kg/s}$
$p$	Pressure of fluid	$\text{Pa}$
$q$	heat flux	$\text{W/m}^2$
$Q$	heat uptake	$\text{W}$
$R$	Radius of pipe	$m$
$S$	Perimeter wetted	$m$
$t$	Time coordinate	$s$
$T$	Temperature (absolute)	$^{\circ}\text{C}$
$u$	Axial flow	$\text{m/s}$
$v$	Radial flow velocity	$\text{m/s}$
$x$	Dryness (steam quality)	–
$z$	Spatial coordinate	$m$

## SUBSCRIPTS

$d$	Diffusion term
$e$	Evaporation
$f$	Flow / Fluid conditions
$p$	Constant pressure (p)
$s$	Source term
$w$	Wall conditions

## ABBREVIATIONS

<i>AVV2</i>	Avedøreværket Unit 2
<i>CFD</i>	Computational Fluid Dynamics
<i>CFL</i>	Courant-Friedrichs-Levy
<i>DONG</i>	Danish Oil and Natural Gas
<i>EOS</i>	Equation of State
<i>FEM</i>	Finite Element Method
<i>IAPWS</i>	International Association for the Properties of Water and Steam
<i>IRBT</i>	Internally rifled boiler tubes
<i>PDE</i>	Partial Differential Equation
<i>SKV3</i>	Skærbækværket Unit 3, Denmark
<i>TSO</i>	Transmission system operator
<i>VHP</i>	Very High Pressure Turbine - Skærbækværket Unit 3, Denmark
<i>WENO</i>	Weighted Essentially Non-Oscillatory

## INTRODUCTION

The deregulation of electricity markets and the massive investments in renewable energy in Europe have increased the request for flexibilization of large central power plants. Denmark was the first country re-

ally to experience the challenges that the stochastic nature of wind impose on the electricity systems. The challenges with renewable sources began in west Denmark as early as around the year 2000 and have ever since just increased as more wind farms have been commissioned. The average generation from renewables in Denmark is some 33.2 % by 2013, according to the annual energy statistics from the Danish TSO (Energinet.dk). In December 2013, wind power for the first time reached a level corresponding to more than half of the electricity consumption (54.8 per cent). The Danish politicians have set the objective of 50 per cent wind power in relation to the electricity consumption by 2020. Looking beyond Denmark's borders, Germany is about to impose even greater challenges up on themselves and their thermal power plants. They have invested massively in renewables, both wind and photovoltaic generation, and plan to have all nuclear generation phased out by 2023. Both Denmark and Germany already have massive challenges with the momentarily balancing of power consumption and generation which is a prerequisite for a stable power system. To balance consumption and generation it is necessary to operate the thermal power plants 'as the wind blows and the sun shines'. The flexibility requirements impose on thermal units are especially:

- The request for lower minimum load such that the units are ready to ramp up if the generation from renewables suddenly fails (e.g. forecast errors)
- The request for faster start-up (again typically forecast errors)
- The request for larger ramping rates (typically because fewer units are in operation but the total demanded load gradient remains the same)

All three flexibilization initiatives mentioned above are important for the inclusion of even more renewables. However, if one digs further into the technical challenges, it becomes clear that the lower stable minimum boiler load is one of the most important issues for the flexibility-optimisation and thus the integration of renewables.

## MOTIVATION

Danish central power plants are all once-through boilers of the Benson type. The water walls are typically constructed of some 200 tubes connected in parallel, running from hopper to furnace outlet with an inclination angle of approximately 15 degrees. Each of these tubes must at any instant be sufficiently cooled at any location along the tube. Normally this corresponds to a tube mass flux rate of 700-800 [kg/s/m<sup>2</sup>] at minimum stable generation and 2000-2500 [kg/s/m<sup>2</sup>] at rated capacity (Effenberger, [1], p. 518). If cooling fails for a certain time, the tube in question will be damaged (material creep and cyclic hoop stress) and eventually burst. Consequently, each power plant has a minimum feed water flow rate, which must be respected in order to avoid trip of the plant. Typically, the boiler is tripped after only 10 seconds, if the flow rate is too low. This trip criterium is very problematic and imposes huge challenges for the control engineer at low load operation, for example, during start-up/shut-down of the second feed pump or during swelling.

## LITERATURE REVIEW

Much effort has been put into modelling evaporators. Focus was especially on the dynamic regulatory technical features of the power plant boilers, but there is not much literature on dynamic modelling of the evaporation process in the power plant boiler and the consequent load limits. There are some references about experimental studies of evaporators, and much of this material is based on standards and is well documented in [7]. In [8] there is the modeling of a complete circuit distribution of a flow network system in a water wall of an ultra-supercritical boiler with vertical tubes. The model is steady, state and good agreement is achieved between the calculated mass flux distribution in the lower front wall and the plant data; the maximum relative difference is between 5.6 and 9.7 %. A dynamic evaporator model, which is able to simulate the entire vaporization process, including the sub-cooled liquid at the entrance and super-heated fluid at the outlet, has not been seen in published literature, due to the complexity around the saturation curve, which basically includes a singularity in the gradient of the density.

With respect to internal rifled boiler tubes (IRBT),

Harald Griem, [9] wrote back in 1985 on the subject, and both KEMA, [10] and Siemens have performed considerable experimental work that is considered proprietary information, see [11] and [12]. Other authors have dealt with the experimental topic, with special focus on smooth and internal rifled boiler tubes; see [13], [14], [15] and [16]. Here consistent algebraic function terms are developed for the frictional pressure drop and heat transfer in smooth and IRBT. A thermo-hydraulic analysis of an ultra-supercritical boiler at full load is performed in [8], but no studies of part load conditions.

## MODEL LAYOUT

The following section presents a mathematical model for both fluid and pipe wall of a circular evaporator.

### 1D - fluid model

A homogeneous model consists of three conservation equations given by (1), (2) and (4), which is formulated in the three non-dependent variables  $\rho$ (density),  $\dot{m}$ (mass flow) and  $E$ (internal energy), where the dependant variables  $z \in [0, \dots, l_z]$  and  $t \in [0, \dots, \infty]$ . For  $\dot{m} = \bar{\rho}uA$  we find:

Continuity equation:

$$\frac{\partial}{\partial t}(\bar{\rho}A) + \frac{\partial}{\partial z}(\dot{m}) = 0 \quad (1)$$

Momentum equation:

$$\frac{1}{A} \frac{\partial}{\partial t}(\dot{m}) + \frac{1}{A} \frac{\partial}{\partial z}(\dot{m}u) = -\frac{\partial \bar{p}}{\partial z} - \bar{\rho}g \cos(\theta) - F_w \quad (2)$$

where  $F_w = \frac{S_w}{A} \tau_w$ , and the wall shear stress ( $\tau_w$ ) is typically expressed as:

$$\tau_w = \frac{1}{2} f_w \rho |u| u. \quad (3)$$

Energy equation:

$$\begin{aligned} \frac{\partial}{\partial t} \left( \bar{\rho}A\bar{h} + \frac{1}{2}\bar{\rho}Au^2 - pA \right) + \frac{\partial}{\partial z} \left( \dot{m}\bar{h} + \dot{m}\frac{1}{2}u^2 \right) \\ = \dot{q}_r S_w - \dot{m}g \cos(\theta). \end{aligned} \quad (4)$$

Then equation (4) can be reformulated by using the definition of the total specific convected energy:  $\bar{e} = \bar{h} + 1/2u^2 + gz \cos(\theta)$ , and by using the continuity equation to eliminate the gravitational terms on the left side, we find:

$$\frac{\partial}{\partial t} (A(\bar{\rho}\bar{e} - \bar{p})) + \frac{\partial}{\partial z} (\dot{m}\bar{e}) = \dot{q}_r S_w - \dot{m}g \cos(\theta) \quad (5)$$

where  $\dot{q}_r$  represents the heat flux per unit surface area through the outer wall of the tube. The internal energy  $E$  is given as:  $E = (\bar{\rho}\bar{e} - \bar{p}) \cdot A$ , which is measured in [J/m].

The independent variable  $t$  represents the time in [s], and  $z$  is the spatial coordinate referring to the flow direction of the fluid given in [m]. The dependent variables are  $\bar{\rho}$ ,  $\dot{m}$  and  $e$ , meaning the fluid density, mass flow and total energy of the conserved fluid, respectively. The pressure can be determined iteratively by water steam tables:  $p = p(e, \bar{\rho})$ .  $A$  is the tube cross-section area, measured in [m<sup>2</sup>]. The source term  $g_s$  consists of both source/sink terms related to gravity- and wall friction forces. The diffusion term  $g_d$  includes a contribution from the mixing length eddy viscosity ( $l^2 = 0.01$  [m<sup>2</sup>/s]), working as a damping term in the vicinity of the saturation line of water. A recommended size of attenuation area is found to be  $x_e \in [-0.01, 0.01]$ . The internal energy  $e$  is given as:  $e = (\rho\bar{E} - p) \cdot A$ , which is measured in [J/m]. Here the fluid temperature  $T_f$  is a function of  $\bar{\rho}$  and  $h$ . The constitutive relations due to the thermodynamic properties are based on IAPWS 97, and are interpolated in a bilinear scheme, described in [5] for minimising the computational work. Note that the gravity is reduced according to the heat pipe inclination ( $\sin(11.4^\circ)$ ) on the SKV3 boiler.

## 1D - pipe wall model

The solution of problems involving heat conduction in solids can, in principle, be reduced to the solution of a single differential equation, the heat conduction equation. As an alternative, we could use a two dimensional model to describe the spatial temperature resolution of the pipe material. The single-layer equation can be derived by making a thermal energy balance on a differential volume element in the solid. A volume element for the case of conduc-

tion only in the  $z$ -direction is illustrated in figure (1).

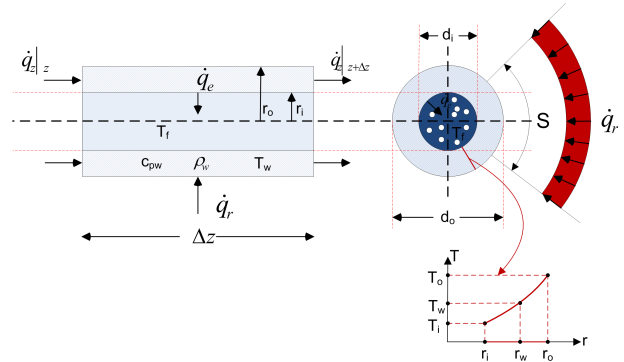


Figure 1: Energy transfer and heat flow terms on a slice of a pipe wall element.

The generation term is set to zero, but could be an electric current or the decay of a radioactive material. The rate at which thermal energy enters the volume element across the face at  $z$  is given by the product of the heat flux and the uniform cross-sectional area,  $\dot{q}_z|_z A_c$ , where  $A_c = \pi(d_o^2 - d_i^2)/4$ . Similarly, the rate at which thermal energy leaves the element across the face at  $z + \Delta z$  is  $\dot{q}_z|_{z+\Delta z} A_c$ . For a homogeneous heat source/sink of strength  $\dot{q}_r$  per unit area, the net rate of generation is  $\dot{q}_r S \Delta z$ , where  $S$  is the pipe perimeter of impact. Finally, the rate of accumulation is given by the time derivative of the thermal energy content of the volume element, which is  $C_{pw} \rho_w (T - T_{ref}) A_c$ , where  $T_{ref}$  is an arbitrary reference temperature. Thus, the balance equation becomes:

$$\Delta z \rho_w C_{pw} A_c \frac{\partial T_w}{\partial t} = (\dot{q}_z|_z - \dot{q}_z|_{z+\Delta z}) A_c + \dot{q}_r S \Delta z - \dot{q}_e d_i \pi \Delta z \quad (6)$$

where  $C_{pw}$  and  $\rho_w$  are the heat capacity and the density of the pipe wall, given by equation (9). By dividing (6) by  $\Delta z$  and letting  $\Delta z \rightarrow 0$ , we get a first-order PDE describing the energy balance in the pipe element as a function of  $t$  and  $z$ .

$$\rho_w C_{pw} A_c \frac{\partial T_w}{\partial t} = -A_c \frac{\partial \dot{q}}{\partial z} + \dot{q}_r S - \dot{q}_e d_i \pi \quad (7)$$

The heat flux  $\dot{q}$  per unit area can be expressed via the Fourier formula:  $\dot{q} = -k_w \frac{\partial T_w}{\partial z}$ , where  $k_w$  is the thermal conductivity measured in [w/mK]. For isotropic

materials, we use the thermal diffusivity given by:  $\alpha = \frac{k_w}{\rho_w C_{pw}}$  in [ $m^2/s$ ], which in a sense is a measure of thermal inertia and expresses how fast heat diffuses through a piece of solid. For a typical panel wall, the thermal diffusivity is approximately  $1.98 \cdot 10^{-6}$  [ $m^2/s$ ] at  $200^\circ C$ ; see [25]. Hence the energy balance for the isotropic pipe wall can be described by:

$$\frac{\partial T_w}{\partial t} = \alpha \frac{\partial^2 T_w}{\partial z^2} + \frac{\dot{q}_r}{\rho_w C_{pw} A_c} \frac{S}{A_c} - \frac{\dot{q}_e}{\rho_w C_{pw} A_c} \frac{d_i \pi}{A_c}, \quad (8)$$

$$z \in [0, l_z] \wedge t \geq 0$$

where  $\dot{q}_r$  is the radiation from the furnace and  $\dot{q}_e$  is the convective heat transfer between the flowing fluid in the pipe and the pipe wall inner surface,  $\dot{q}_e = h(T_w - T_f)$ . The convective heat transfer coefficient is named  $h$ , and the driving temperature difference is given by the temperature difference between the wall mean temperature ( $T_w$ ), outlined in equation (10), and the mixture fluid temperature ( $T_f$ ). For isotropic materials, we have expressions of  $C_{pw}$ ,  $k_w$  and  $\rho_w$  as a function of temperature in Kelvin from [25] and [26]:

$$C_{pw} = 6.683 + 0.04906 \cdot T + 80.74 \cdot \ln(T) \text{ [J/kgK]}$$

$$k_w = 9.705 + 0.00176 \cdot T - 1.60 \cdot 10^{-6} \cdot T^2 \text{ [w/mK]} \quad (9)$$

$$\rho_w = 7850 \text{ [kg/m}^3\text{]} \text{ at } 20^\circ C \text{ for 13CrMo44}$$

and the wall mean temperature is estimated to:

$$T_w = \frac{1}{A_c} \int_{r_i}^{r_o} 2\pi r \cdot T(r) dr \quad (10)$$

$$= a_1 \cdot T_i + (1 - a_1) \cdot T_o$$

where  $T(r)$  is given by (17) and  $a_1$  is given by

$$a_1 = \frac{r_i^2}{r_i^2 - r_o^2} - \frac{1}{2 \ln(r_i/r_o)} \quad (11)$$

The wall density is assumed constant in temperature  $T$ . A simple, fast and robust model of the heat transfer in film boiling is given by [27]. The heat transfer coefficient  $h_{fb}$  is given by equation (12). The single-phase laminar heat transfer coefficient is calculated from equation (14).

$$\alpha = c_1 \dot{q}^{0.673} \text{ [W/m}^2\text{K]} \quad (12)$$

where the coefficient  $c_1$  is given as

$$c_1 = \frac{0.06136}{\left[1 - \left(\frac{T_s}{378.64}\right)^{0.0025}\right]^{0.73}} \quad (13)$$

The single phase laminar heat transfer coefficients is calculated from

$$Nu_s = \frac{h_s d_i}{k_f}$$

$$= 4.36 \quad (14)$$

The total heat transfer coefficient is given by (15), and consists of two contributions: one from the convective heat transfer boundary layer associated to the flowing fluid inside the heat pipe and one that relates to conduction through the pipe wall material:

$$h = \frac{1}{\frac{1}{h_c} + \frac{r_i}{k_w} \cdot \ln(r_w/r_i)} \quad (15)$$

where  $h_c$  expresses the heat transfer coefficient due to the thermal boundary on the inner side of the pipe wall and  $r_w$  is defined by  $T_w = T(r_w)_z$ .  $h_c$  is smoothed in-between  $h_s$  and  $h_{fb}$  depending of the dryness ( $x$ ) of the fluid.

$$h_c = \begin{cases} h_s & \text{for } x > 1 \vee x < 0 \\ h_{fb} & \text{for } 0 \geq x \geq 1 \end{cases} \quad (16)$$

Additionally,  $h_c$  is adjusted on the basis of a smoothing between laminar and turbulent single-phase flow as well as for two-phase flow. The smoothing function is described in [2] and is of second-order. The associated slopes are determined numerically. Since we use the calculated average wall tube temperature as the driver in the calculation of the total heat transport to the fluid, we must know  $r_w$ . Due to the knowledge of radial conduction in the pipe, we use a simple analytical wall temperature profile for estimating the inner wall temperature, expressed by the averaged wall temperature ( $T_w$ ), based on the heat transfer through the isotropic pipe wall to the flowing fluid given by equation (10). Let  $T(r)_z$  represent the radial temperature distribution in the isotropic pipe wall by, which can be rewritten as

$$T(r)_z = a_0 \ln\left(\frac{r}{r_o}\right) + T_o \quad (17)$$

where  $a_0 = \frac{T_i - T_o}{\ln(r_i/r_o)}$  and  $r$  is the pipe radius with suffix (i=inner) and (o=outer). Hence, for small values of the thermal diffusivity, the averaged wall temperature can reasonably be estimated by equation (10). Hence the entire heat transfer can be estimated for the temperature range in-between the wall

mean temperature ( $T_w$ ) and the fluid mixture temperature ( $T_f$ ), which is assumed homogeneous and well mixed with a temperature boundary layer represented by  $h_c$ . The one dimensional pipe wall model only consists of the axial heat transfer term, and has no spatial resolution in the radial dimension. The inner wall temperature ( $T_i$ ) can be determined by use of the equation for pure conduction through the pipe:

$$\dot{q}_r S = \frac{2\pi k_w}{\ln(r_o/r_i)}(T_o - T_i) = \frac{2\pi k_w}{\ln(r_w/r_i)}(T_w - T_i) \quad [w/m]. \quad (18)$$

Hence we find  $T_i$  by insertion (17) in (18):

$$T_i = T_w - \frac{q_r S \ln\left(\frac{r_o}{r_i}\right)(1 - a_1)}{2\pi k_w} \quad (19)$$

where  $a_1$  is given by equation (11). Hence  $r_w$  in (15) can be determined from (17) and (19) and we find

$$\begin{aligned} h &= \frac{1}{\frac{1}{h_c} + \frac{r_i(a_1-1)}{k_w} \cdot \ln(r_i/r_o)} \\ &= \frac{1}{\frac{1}{h_c} + \frac{r_i}{k_w} \cdot \ln(r_w/r_i)} \end{aligned} \quad (20)$$

Note that the heat flux is positive for  $T_i > T_f$ . Using the model parameters for the panel wall of SKV3 (from table (1)), we find  $a_1=0.423$  and the temperature fall above the pipe wall is:  $T_o-T_i=27.9$  [ $^{\circ}C$ ], which gives a temperature gradient in the pipe wall of  $dT/dr= 3930$  [ $^{\circ}C/m$ ] for a heat flux of  $\dot{q}_e=100$  [ $kW/m^2$ ]. The heat conduction in the material is the most significant barrier for an effective cooling of the tube wall.

## MODEL SETUP

A homogeneous model, is described in this article and is solved using the numerical algorithms based on a fifth-order WENO scheme, with corresponding diffusion and source term. The numerical method is briefly outlined in the Appendix and consists of 400 computational points with a CFL number of 0.8. A third-order TVD time integrator is used, for reasons of ensuring a high numerical stability as well as minimizing the time-consumption in the calculations. The numerical scheme is tested for consistency and stability with respect to both a scalar model and a system of hyperbolic equations

and both have been successfully compared to analytical results, from the literature as well as other published results. This work is outlined and published in [5]. Three Dirichlet boundary conditions are applied for the hydraulic case and two Neumann boundaries are applied for the thermal pipe wall model, given as zero gradients in the wall temperature at each pipe end (no heat loss).

The intention is to model an evaporator, that can induce pressure and density oscillations initiated by the compressibility, arising as a result of a phase shift in the lower part of the evaporator. Therefore, we apply a constant downstream Dirichlet pressure boundary condition that corresponds to a stiff system downstream the evaporator tube, meaning without any pressure absorption effects from compressibility in the downstream turbine system. A good analogy for this is a geyser, with a constant surface pressure and an intense heat absorption in the bottom region, whereby an oscillating pressure wave is initiated due to the compressibility and density reduction of the fluid, caused by intense heat from the underground. Additionally we force the model with both a constant enthalpy and mass flux located on the upstream boundary, supplied by a heat flux profile along the entire heat pipe.

The model is gently started (soft start) in two steps: at  $t=0$  [s] the pure hydraulic model is gently started over 4 seconds, without heat flux. After ten seconds of simulation, the heat flux is built-up during four seconds to  $100$  [ $kW/m^2$ ], in accordance with the operating observations obtained at SKV3. This is done to avoid heavy shock waves moving forward and back in the entire solution domain. The computational results are stored as line series for an equidistant time step and as time series at two stations, located at  $z_A=\frac{l_z}{8}$  and  $z_B=\frac{7l_z}{8}$ , named stations A and B, respectively, where  $l_z$  is the total tube length.

The dynamic start-up process for a constant linear heat flux profile can be seen in figures (2) and (3), where the density is given in [ $kg/m^3$ ], pressure in [bar], temperature in [ $^{\circ}C$ ], enthalpy in [kJ/kg] and mixture velocity in [m/s].

Note that the temperature curves for the fluid and the pipe wall both refer to the same temperature

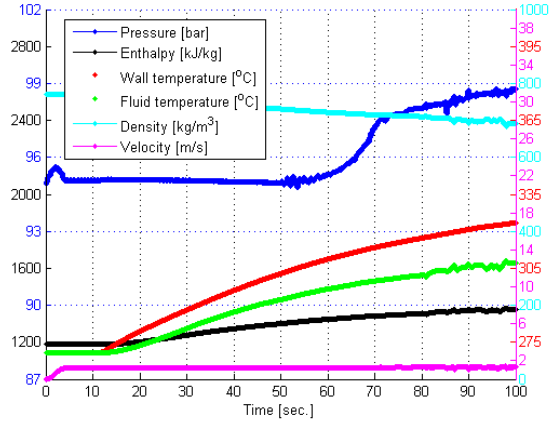


Figure 2: Soft start response of SKV3 evaporator model @ station A.

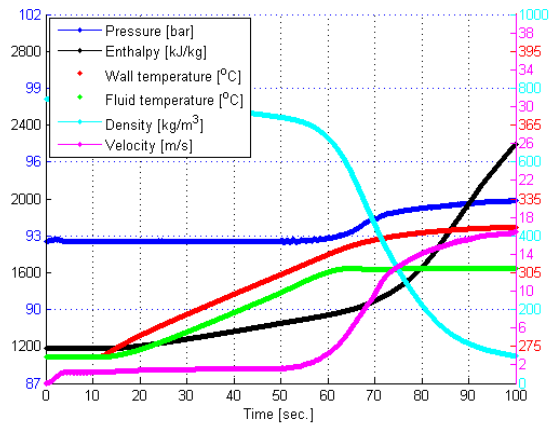


Figure 3: Soft start response of SKV3 evaporator model @ station B.

scale corresponding to the red fluid temperature scale on the right-hand side of the graph. This fact is applied in the whole paper. The soft start model is based on a third-order theory outlined in [2], which gives a  $C^2$  continuous sequence, which means zero gradients of the first derivative at both ends of the soft start period. The *system of balance laws* (SBL) for the evaporator model is given in a compact vector notation:

$$\begin{aligned} \frac{\partial \Phi(z,t)}{\partial t} + \frac{\partial f(\Phi(z,t))}{\partial z} &= \mathbf{g}_s(\Phi(z,t)) \quad (21) \\ &+ \mathbf{g}_d \left( \frac{\partial \Phi}{\partial z}, \Phi(z,t) \right), \\ \Phi &\in \mathbb{R}^m, m=4, \quad t \geq 0 \wedge z \in \Omega \end{aligned}$$

where the dependent variable  $\Phi$  and the flux vector  $f$  are given as:

$$\Phi = \begin{pmatrix} \bar{\rho}A \\ \dot{m} \\ \bar{e} \\ T_w \end{pmatrix}, \quad f(\Phi) = \begin{pmatrix} \dot{m} \\ \frac{\dot{m}^2}{\bar{\rho}A} + \bar{\rho}A \\ \frac{(\bar{e} + \bar{\rho}A)\dot{m}}{\bar{\rho}A} \\ 0 \end{pmatrix}$$

and the source and diffusion vector are given as:

$$\mathbf{g}_s(\Phi) = \begin{pmatrix} 0 \\ \bar{p} \frac{\partial A}{\partial z} - \bar{\rho} g A \cos \theta - \sqrt{\frac{\pi}{A}} f_w \frac{\dot{m}|\dot{m}|}{\bar{\rho}A} \\ S_w \dot{q}_e - \dot{m} g \cos(\theta) \\ \frac{\dot{q}_r}{\rho_w C_{pw} A} - \frac{\dot{q}_e}{\rho_w C_{pw} A} \end{pmatrix} \quad \text{and}$$

$$\mathbf{g}_d(\Phi) = \begin{pmatrix} 0 \\ \frac{l^2 S_w}{\bar{\rho}A^3} \frac{\partial \dot{m}^2}{\partial z^2} \\ 0 \\ \alpha \frac{\partial^2 T_w}{\partial z^2} \end{pmatrix}$$

The independent variable  $t$  represents the time in [s], and  $z$  is the spatial coordinate referring to the flow direction of the fluid given in [m]. The dependent variables are  $\bar{\rho}$ ,  $\dot{m}$  and  $e$ , meaning the fluid density, mass flow and total energy of the conserved fluid, respectively. The pressure can be determined iteratively by water steam tables:  $p = p(e, \bar{\rho})$ .  $A$  is the tube cross-section area, measured in [ $m^2$ ]. The source term  $\mathbf{g}_s$  consists of both source/sink terms related to gravity- and wall friction forces. The diffusion term  $\mathbf{g}_d$  includes a contribution from the mixing length eddy viscosity ( $l^2=0.01$  [ $m^2/s$ ]), working as a damping term in the vicinity of the saturation line of water. A recommended size of attenuation

area is found to be  $x_e \in [-0.01, 0.01]$ . Here the fluid temperature  $T_f$  is a function of  $\bar{p}$  and  $h$ . The constitutive relations due to the thermodynamic properties are based on IAPWS 97. To improve the computational speed it is recommended to use a bilinear interpolation; see [5], where we create a look-up table within approximately 160000 nodes, which ensures an accuracy below 4% as an absolute maximum, due to a smoothing of the interpolated properties in the vicinity of the saturation line. It is only in the vicinity of the saturation line of water, where we experience a significant error; otherwise the averaged relative error is below 0.3%.

Parameter	Value	Unit
Gravity (g) - projected	1.9399	[m/s <sup>2</sup> ]
Spatial start position	0.000	[m]
Spatial end position (L)	193.499	[m]
Inner diameter of pipe ( $d_i$ )	23.8	[mm]
Outer diameter of pipe ( $d_o$ )	38.0	[mm]
Heat conductivity in wall ( $k_w$ )	20.278	[w/mK]
Wall density ( $\rho_w$ )	7850.0	[kg/m <sup>3</sup> ]
Specific heat capacity of pipe wall ( $C_{p_w}$ )	527.21	[J/kg/K]
Heat flux ( $\dot{q}_e$ )	100.0	[kW/m <sup>2</sup> ]
Wall roughness ( $\lambda$ )	1.0E-6	[m]
Initial Enthalpy - left side	1187.6988	[kJ/kg]
Initial Enthalpy - right side	1187.6988	[kJ/kg]
Initial Pressure - left side	92.3762	[Bar]
Initial Pressure - right side	92.3762	[Bar]
Initial Velocity - left side	0.0	[m/s]
Initial Velocity - right side	0.0	[m/s]
Pressure BC (Dirichlet - right side)	92.3762	[Bar]
Enthalpy BC (Dirichlet - left side)	1187.6988	[kJ/kg]
Velocity BC (Dirichlet - left side)	1.1711	[m/s]
Simulation time	400.0	[s]
Output frequency	0.1	[s]
CFL number	0.80	[-]
Number of computational grids ( $N_p$ )	400	[-]
Slip Correction Factor	1.0	[-]

Table 1: Geometrical and numerical specifications for SKV3 heat pipe.

## Model calibration

The hydraulic model is calibrated in relation to the static operating data, which are available from SKV3; see table (2).

Sample nr.	$\dot{m}$	$h_{in}$	$h_{out}$	$\dot{q}$	$P_{in}$	$P_{out}$	$\Delta p$	Load
Units	[kg/s]	[kJ/kg]	[kJ/kg]	[MW]	[bar]	[bar]	[bar]	[%]
1	195.46	1514.27	2894.32	269.75	244.20	230.05	14.15	80.5
2	258.11	1566.09	2835.05	335.27	325.20	306.29	18.91	100.0
3	89.54	1169.20	2819.71	140.48	110.89	105.58	5.31	41.9
4	90.04	1187.70	2720.25	137.99	96.87	92.38	4.49	41.2

Table 2: Mean values for heat and pressure balance for four samples at SKV3.

As a basis we focus on a model that works in part load, i.e., where we simulate the entire two-phase process in the evaporator, including sub-cooling and superheating. We aimed as a basis for the calibration simulation a heat flux value of approximately 83.8 [kW/m<sup>2</sup>], according to the average flux received by the evaporator in sample 4. The only calibration parameter we are dealing with, is the wall friction, which is determined by a hydraulically smooth industrial boiler tube (The surface roughness is negligible.) The tube length is estimated to be a total of 193.5 m, including various bends and junction boxes. We calculate the upstream pressure in the steady state condition to approximately 97.5 [bar]±0.2 [bar], which approximately corresponds to the measured upstream pressure in sample 4, 96.87 [bar], - a deviation of approximately 0.5 [bar] for hydraulic smooth pipes. Note that the calculated pressure drop is very sensitive to the specified velocity boundary condition. There appears, however, minor pressure oscillations on the upstream boundary, initiated by a phase shift in the vicinity of the transition area to the two-phase region. Basically, the downstream condition should also reflect the measured static outlet enthalpy of 2764.38 [kJ/kg] and a corresponding steady state mass flow, even before the requirement of static energy balance is fulfilled. Here we are only slightly below the average measured static values, corresponding to an enthalpy of 2701 [kJ/kg] and a mass flow of 0.3807 [kg/s] at the very first computational cell versus 0.3816 [kg/s] at the very last computational cell. Based on the above considerations, we can conclude that the model meet our observations in table (2) (sample 4), although the model is not at completely steady state.

We can see from figure (11) that, e.g., the pressure signal contains oscillations, and the corresponding frequency components are difficult to identify. The signal can be analysed using FFT to find the frequency components of a signal in the time domain. The Matlab FFT spectral density analysis is carried out on a subset of the time series in station B, based on a close-up of the pressure time series measured from 150 [s] to 155 [s] of simulation. We can see that the pressure fluctuations primarily consists of a class of waves with frequencies of  $f' \approx 0.25 \cdot n$  [Hz] and with decreasing intensity, where  $n$  is a positive integer. This very low frequency periodic process can be classified as pressure-drop oscillations due to

the dynamic interaction between channel and compressible specific volume in the fluid. The maximum wave-length is given by the length of the tube,  $l_z=193.5$  [m] and the corresponding phase velocity  $u_f=\lambda \cdot f' \cdot n = l_z \cdot 0.25 \cdot n = 48.4 \cdot n$  [m/s]. From figure (10) we can see that the pressure waves are initiated only 10% upstream the tube which corresponds to a standing wave with a phase velocity of  $48.4 \cdot n$  [m/s]. It is interesting to see that the phase velocity can be identified within the orders of magnitude of the estimated speed of sound in a two-phase flow (250 m/s to 868 m/s @ 95 bar), based on the eigenvalue analysis of the two-layer fluid model developed in the Ph.D. thesis in [5].

### Dynamic flow stability

The developed dynamic model is applicable for very different thermo-hydraulic problems, and we analyse four different heat flux distributions on the evaporator tube during the start-up phase, where we observe different dynamic pressure responses. The results that are presented in here, are not as clear as expected, but we can observe that start-up of the boiler, from zero flow to full combustion in part load [100 kW/m<sup>2</sup>], can lead to slightly different dynamic response from the boiler, when changing firing profile at constant heat uptake as well as reduce the operation pressure of the evaporator. We see a higher degree of density fluctuations upstream the boiler, when low firing is applied, while top firing causes more heat-related fluctuations downstream the evaporator (temperature and enthalpy). The applied load gradients are larger than those we see in the real world; see figure (29) and (30). Also the restrictions with respect to reduced lifetime of thick-walled components, like junction boxes or valves, are not taken into account in this analysis.

Last, we touch upon a situation related to the major challenges that the traditional thermal power plants are facing, in connection with the introduction of renewable energy (sun and wind). With the close bond between district heating and electricity production, which is characterized by a so-called back-pressure plant, it is tempting to reduce the live steam pressure and bypass the high-pressure turbines and thus reduce both electricity production and the evaporator pressure. We see from the calculations that we obviously have a significant

pressure drop in the evaporator. The low-pressure evaporator simulation, with an exit pressure of 46 [bar] compared to a normal pressure of 90 [bar], shows a stable response, which after 180 [s] is in a steady state condition; see figures (23) to (25). The pressure loss is approximately 18 [bar]. It is interesting to see that the homogeneous model takes into account the load gradients of pressure and enthalpy, which can initiate the thermal slugs. It is also interesting to note the presence of thermo slugs in the homogeneous evaporator model. The model is able to resolve the sometimes steep gradients in the tubes, which demonstrates that violent slugs really exist at low operating pressures - even in a homogeneous model.

### HEAT FLUX PROFILES

Here follow calculations for investigating how different heat flux profiles affect the dynamics of an evaporator during a start-up period. It is interesting to examine how the flux distribution in a boiler affects the start-up process in a power plant evaporator. Operational experience from SKV3 indicates major start-up problems, which is attempted to be reduced by firing with the top burner floor. We will investigate this in the following, where we examine the dynamic response from the evaporator by four different heat flux profiles. We use a moderate flux distribution coefficient, corresponding to a maximum redistribution of the heat flux of 10% ( $\Delta q = 0.1$ ), meaning that the heat flux profile along the tube is altered a maximum of 20 %.

### Constant heat flux profile

A constant heat flux profile indicates a constant heat flux on the panel wall, which results in a corresponding effective cooling of the pipe wall and can be used as a reference calculation for the study of different flux profiles. This scenario is of academic interest and reveals a more gentle impact of the evaporator. A constant heat flux profile in the evaporator string is illustrated in figure (4).

The numerical model is configured according to table (1), and the heat flux is specified to 100 [kW/m<sup>2</sup>]. A close to static solution is obtained after approximately 400 seconds, and is depicted in figure (5), although a static solution is a truth with

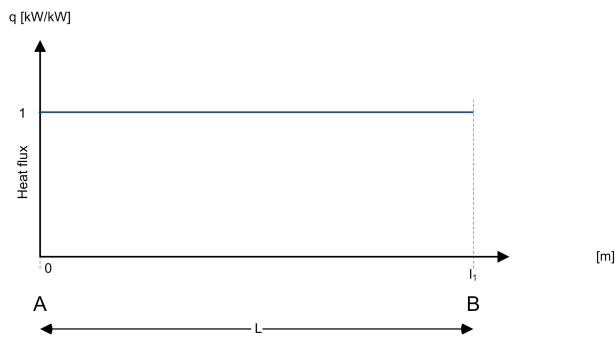


Figure 4: Constant heat flux to boiler.

modifications. Small perturbations in pressure and density are constantly induced, because the model is successively fed with the pressure oscillations created from the transition zone of the sub-cooled to the two-phase fluid, where the very large density gradients occur. These oscillations are controlled by artificial diffusion due to the local turbulence model in the area of transition from single to two-phase flow as well as a smoothing of the EOS along the saturation lines. The results show how the state of the fluid gradually moves from the inlet condition, in the form of sub-cooled water, to the two-phase zone, in which the boiling is starting, and finally reaches the super-heating zone, where the dry steam is superheated to about 385 °C. The pressure drop is fixed downstream in the form of a Dirichlet boundary condition, corresponding to measured pressure levels from (SKV3). The pressure distribution along the evaporator reflects different pressure loss models, the pressure gradient of single and two-phase regions, respectively. The two-phase region makes use of the two-phase multiplier outlined in [6], which multiplies the pressure gradient with up to 16 times relative to the pressure gradient for saturated water. The inlet velocity is specified as an upstream Dirichlet boundary condition, and is soft started by use of the before-mentioned smooth function, having a soft start period of four seconds. This ensures a smooth hydraulic flow condition of the cold evaporator. After wards, the heating is built up smoothly, applied by the same smoothing technique, so that undesirable thermal shock phenomena are avoided. The super-heated steam leaves the downstream boundary at a steady state flow condition with a speed of approximately 24 [m/s]. Pressure oscillations occur as a result of large upstream fluid compressibility in the flow boiling system; see [17],

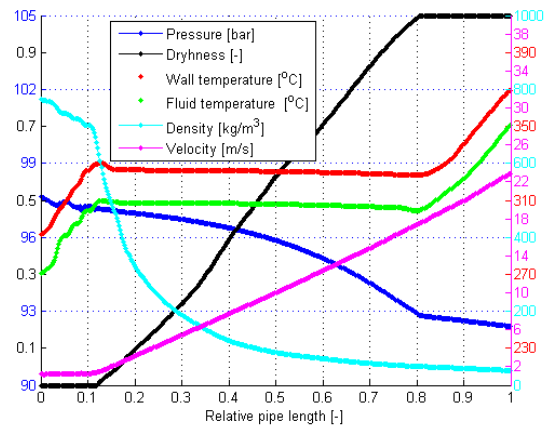


Figure 5: Solutions of SKV3 evaporator model after (R) 400 [s].

[18]. These pressure oscillations appear in the form of pressure fluctuations, arising from the singularity we experience in the gradient field of the fluid density, when saturation is approached and can be generated in the form of a standing wave in front of the boiling zone of the fluid. The dryness line in figure (5) expresses the mass based percentage of the steam flowing in the evaporator tube; not surprisingly, this process is linearly varying and corresponds to a constant heat flux along the tube.

By reducing the number of computational cells to, e.g., 50 elements, without adjusting the artificial diffusion, one would observe a more intensive standing wave at the entrance of the two-phase region, due to intensive heating of the differential cell in the vicinity of the boiling zone, where we have an intensive negative slope in the density as a function of the enthalpy; hence the density change becomes so violent that a pressure wave is established to ensure momentum balance.

### Linear heat flux profile with bottom firing

Operating experience from the SKV3 says that there are inconveniences in the evaporator during start-up when firing low, i.e., when the lower burner roofs are in action during start-up. This enables us to model, by assuming a stylistic heat flux profile, and implement a dynamic thermal hydraulic calculation based on the homogeneous flow model. The profile is illustrated in figure (6), with  $\Delta q = 0.1$ .

Physically this can lead to massive slug formations

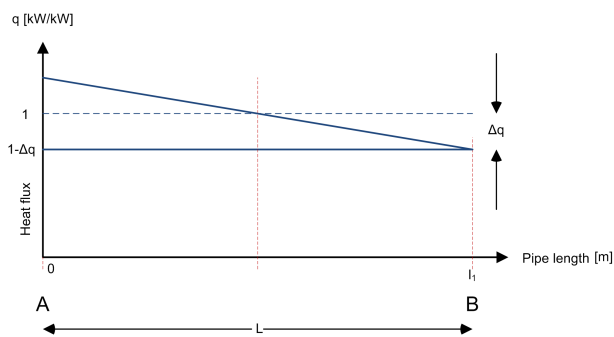


Figure 6: Bottom firing in boiler - linear heat flux to boiler with  $\Delta q=0.1$ .

(pressure and density). We have eyewitness reports from operational staff at SKV3 about how the high-pressure steam line from the evaporator during start-up has moved up to 1/2 meter and in this context has destroyed the insulation around the HP-pipe line and also damaged the associated thermocouples. It is violent forces that are at play, when provoked slugs in the form of density waves or pressure surges act in the steam pipes. Figure (14) shows a dryness profile, which differs from the corresponding simulation with a constant heat flux profile. The difference reflects that the bottom firing case has not yet reached a steady-state condition, and thus is slower to settle into a stable plateau. This emphasizes that the two time series, as illustrated in figures (12 and 13), after 110 [s] from the start of simulation, show considerable density fluctuations in station A and both a strong temperature and a velocity fluctuation in station B. The temperature fluctuations in station B are damped towards the end of the simulation and become stable around 330 [°C]. Note that both the tube wall temperature and the fluid temperature refer to the same temperature scale on the right axis of figures (12 and 13). Especially temperature fluctuations may be critical with respect to the fatigue of pipe material in general, especially when we draw attention to the material structures on the inner surface of the tube, which are extremely sensitive to temperature fluctuations, due to a short time constant in the evaporator tube. This is compensated to some extent by the thermal diffusion, which smooths the temperature distribution in the pipe wall, here illustrated as an averaged wall temperature. This phenomenon may be an early-stage cracking, particularly in the super-heaters, in which the steam temperature is considerably higher.

### Linear heat flux profile with top firing

Operating experience from the SKV3 in particular indicates a greater stability in the evaporator, when the firing is intensified in the top of the boiler. We attempt to model this using a linear heating profile, with the highest heat flux at the top of the boiler. The profile is illustrated in figure (7) and the boiler specifications are similar to the previous setup, except for the reverse heat flux slope with  $\Delta q=0.1$ .

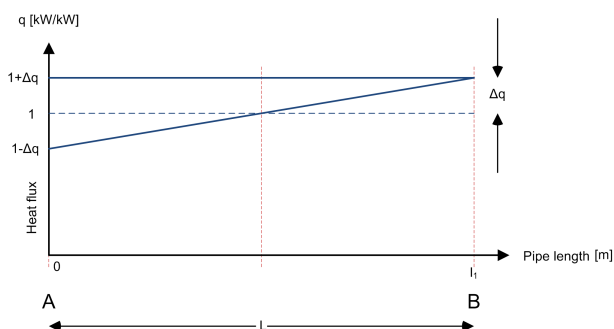


Figure 7: Top firing in boiler with linear heat flux to boiler.

Figure (15) shows an instant picture of the thermodynamic properties of the fluid in the pipe after 200 [s] of real time from the start of the boiler. It is noteworthy that the steam quality is progressing nearly linearly through the evaporator, but has not yet reached a steady state condition. The outlet temperature of the steam is slightly higher than the scenario with low firing. Similarly, we can see a significant difference in both the pressure and the velocity profile compared to the situation with low combustion in the boiler room. The inlet pressure is here approximately 1.5 bar lower, and the steam outlet velocity is only 21 [m/s] compared to 23 [m/s] for the scenario with low firing. Also in this scenario one can see violent fluid temperature fluctuations downstream at station B.

### Parabolic heat flux profile with (parabolic firing)

In accordance with the CFD studies carried out in Chapter [5], we can correlate the flux distribution according to a parabolic profile, so that the flux intensity is greatest around the centre point of the burner zone, which for SKV3 consists of the four burner floors. It should be noted that the maximum value of

the flux intensity, is somewhat above the centre point of the burner system. A parabolic heat flux profile in an evaporator string is illustrated in figure (8) as a relative flux distribution profile and can be idealised

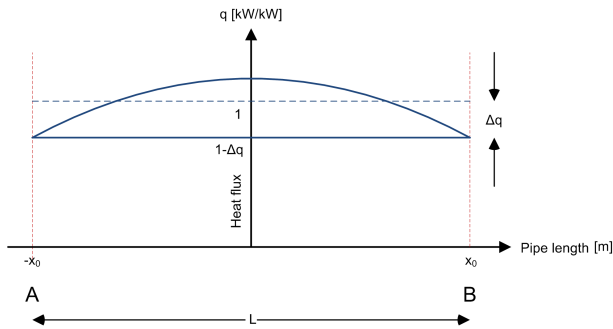


Figure 8: Normal firing in boiler with weak parabolic heat flux to boiler.

as a second-order symmetrical profile, given by

$$q^*(x) = a \cdot (x + x_0)(x - x_0) + b, \quad b = 1 - \Delta q. \quad (22)$$

A simple requirement for the distribution function is that the integral of the distribution function over the entire interval of definition must be of unity, so that we do not add more energy than expected for the evaporator tube. We can thus ensure that the distribution function has the desired functionality by requiring:

$$\begin{aligned} \int_{-x_0}^{x_0} q^*(x) dx &= 2x_0 \cdot 1 & (23) \\ &= \int_{-x_0}^{x_0} (a \cdot (x + x_0)(x - x_0) + b) dx \\ &= -\frac{4a}{3}x_0^3 + 2bx_0 \end{aligned}$$

Hence the coefficient can be estimated to

$$a = -\frac{\Delta q}{x_0^2} \quad (24)$$

and for  $x_0=1$ , the equation (22) can be formulated as

$$q^*(x) = \frac{3\Delta q}{2} \cdot (1 - x^{*2}) + 1 - \Delta q, \quad x^* \in [-1, +1] \quad (25)$$

wherein  $x^*$  is a dimensionless position in the evaporator. We can see that the maximum flux occurs at  $x^* = 0$ , corresponding to  $q^* = 1 + \Delta q / 2$ . Similarly, the minimum flux attached to the top and the bottom of the evaporator for  $x^* = \pm x_0$ , respectively. Here we find  $q^*(\pm x_0) = 1 - \Delta q$ . We can again observe an almost linear relationship between steam quality and

pipe length, corresponding to a distinct stable heat absorption. The outlet temperature of the evaporator is the lowest of all scenarios, and the inlet pressure corresponds to the scenario with constant heat flux. This reflects that the models are not in dynamic equilibrium, since all scenarios receive the same effect and the heat flux profile is almost linear.

## COMPARISON OF THE FLUX PROFILES IN HIGH PRESSURE EVAPORATOR

The start-up process with different heat flux profiles causes different dynamic pressure responses. As shown in the figure (31) for station A, one observes different pressure build-ups, where we clearly can see that the low combustion causes a faster and steeper pressure build-up than the other profiles, so that the top firing causes the smallest pressure build-up. Immediately thereafter, the response of the more or less homogeneous pressure build-up, is replaced by a more oscillating process, where the moving average gradually decreases over time. All four scenarios have an oscillating response; however, there is a trend to bottom firing have a more moderate exit amplitude. In station B we almost see identical pressure structures, but with varying timing. The bottom firing scenario flattens out soon and settles at a stable level, while the top firing scenario flattens out later and also attempts a second pressure build-up, but quickly falls back to the final level of the downstream pressure. When we look at the time series of enthalpy in station A, there is no significant difference observable among the four scenarios. Downstream station B, a time delay occurs of the enthalpy front, and not surprisingly, we see the fastest enthalpy front for low firing, while high firing has the slowest front; see figure (32). After 80 [s] of simulation we see a gradually more oscillating density-wave in station A, see figure (33), which dominates the rest of the simulation period. In station B we see a significantly higher density for the bottom firing scenario, but with a lower degree of oscillation compared to the other scenarios. Here we find surprisingly the greatest density oscillations in the top firing scenario. The fluid temperature is illustrated in figure (34). In station A there is a steeper increase in fluid temperature for the low firing scenario, which ends on the same level as for the other scenarios, due to the entrance to the two-phase region (almost identical saturation pressure).

In station B, we conversely see the largest temperature gradient before the two-phase region for top firing, and again, the temperature ends at the same level, as entering the two-phase region. In the superheated region, we again see drastic temperature fluctuations, surprisingly most notably for the high-fired scenarios. The observed momentary temperature fluctuations are above 20 degrees, for the top-firing scenario. The associated material temperature is dampened much, compared to the fluid temperature, and here we see the highest material temperature in the bottom firing scenario, with a difference of approximately 10 [°C] compared to the top firing scenario. The material temperatures are illustrated in figure (35). At station A, we can see a significantly higher material temperature (+3 [°C]) for the bottom-firing scenario, compared to the other scenarios.

## LOW-PRESSURE EVAPORATORS

During the last decade, Danish utilities (Vattenfall AB and DONG Energy A/S) have invested much effort in the optimisation of thermal power plants in order to outbalance the fluctuations imposed by wind and sun. One could argue that we could phase out the existing thermal plants and switch to open pass gas turbines to solve the problem, but this is a rather expensive solution because we have a fleet of quite new super-critical power plants that still have a significant life time. Simultaneously, the power stations are committed to supply district heating to a large customer base. This means that there is a strong link between the production of district heating and electricity, which can result in a significant overproduction of electricity, when the weather is cold and windy. This can be accomplished by, for example, reducing the outlet pressure of the SKV3 evaporator, while bypassing the VHP turbine, so that the pressure of the evaporator is aligned with the HP turbine. Bypassing the VHP turbine at low load corresponds to an evaporator pressure decrease from approximately 90 [bar] to 46 [bar] at the evaporator outlet. This leads to less power output without compromising the district heating production, but the unit efficiency deteriorates.

In this part of the article, we examine how a power plant evaporator (SKV3) with smooth pipes behaves, when the boiler outlet pressure is reduced

considerably below the normal circulation pressure for Benson boilers. Four simulations with different firing profiles are performed, so that the sensitivity to uneven heating can be assessed. Note that the applied input enthalpy (boundary condition) is unchanged relative to the previous calculations. This results in minimal sub-cooling, though sub-cooling still exists. In practice this can lead to mal-distribution problems.

## Heat flux profiles

Here we carry out calculations with the aim of investigating how different heat flux profiles affect the dynamics of a low-pressure configuration of the SKV3 evaporator during a dynamic start-up period of 200 [s]. Again we use the four different profiles: a constant heat flux on the panel wall as illustrated by figure (4), a linear profile representing situations with bottom firing of the boiler as illustrated in figure (6), a parabolic heat flux profile in the evaporator string as illustrated in figure (8) and finally a linear profile representing situations with top firing of the boiler as illustrated in figure (7).

## Constant heat flux profile

This scenario is again of academic interest and involves a more gentle impact of the evaporator. The outcome of the linear heat flux simulation shows a very stable evaporator, illustrated in figure (16), with a very high pressure drop (15.7 [bar]) and an outlet steam velocity of 48 [m/s], which is very high. The steam quality profile is perfectly linear along the pipe, indicating a constant and stable heat uptake. The corresponding time series at station A and B are illustrated in figures (17) and (18). There occur violent pressure oscillations in connection with the start-up of the model, and the model is first stabilized after approximately 140 [s]. The pressure oscillations achieve a size of up to 5.5 [bar] and thus may be critical in the supply of steam for each evaporator tube (mal-distribution). These oscillations occur in combination with enthalpy fluctuations and affect the flow velocity, which momentarily may rise 10 [m/s] within a period of less than one second. We can thus conclude that the start-up period in a low-pressure evaporator is a violent dynamical phenomenon for the first approximately 140 [s] of simulation.

### **Linear heat flux profile with bottom firing**

Experience from earlier simulations has shown that bottom firing leads to higher dynamic instability in the evaporator, and is no exception in this situation with reduced evaporator pressure. After 200 [s] we see a steady state picture of the axial profile of the thermo-hydraulic properties; see figure (19). As shown in figure (20), the system reaches a steady state condition after more than 160 [s] from the start, whereas the scenario with linear heat flux uses 140 [s] to reach steady state. At the upstream station we see the same tendencies, but with less oscillations; see figure (21). The dynamic transients are also more violent here, where the fluid velocity fluctuates dramatically (up to 15 [m/s] in less than one second). The pressure fluctuates violently, too, but falls quickly into a plateau after only 100 [s] after start-up. The fluid velocity and enthalpy oscillations are dampened gradually, until a steady state situation is reached after 160 [s] from the start. This indicates that at a lower evaporator pressure, there is a greater compressibility in the evaporator, with a steeper negative gradient in the density, while entering the two-phase region. Operating experience from the SKV3 reveals that there are evaporator instabilities during start-up when firing low, i.e., when the lower burner rows are in action during start-up. This tendency is strengthened when the evaporator pressure is reduced.

### **Linear heat flux profile with top firing**

Operating experience from the SKV3 in particular indicates a greater stability in the evaporator, when the firing is intensified in the top of the boiler. We attempt to model this using a linear heating profile, with the highest heat flux at the top of the furnace. The lower operation pressure leads to a high degree of stability after 200 [s].

Figure (22) shows how the thermodynamic properties of the fluid change along the pipe, for the top firing scenario. It is worth noting that the enthalpy increases linearly with the length of the tube, with no enthalpy slugs at all, which indicates a high level of stability in the production of the superheated steam. Similarly, we can see a significant difference in both the pressure and the velocity profile compared to the situation with low combustion in the furnace. The

pressure is here approximately 0.5 [bar] lower and the steam outlet velocity is here similar, 47 [m/s] against 48 [m/s] in the first scenario. The time series in stations A and B (figures 24 and 25) show an unstable start-up process of the evaporator, with stable conditions after 140 [s] from the start. This means that top firing appears more stable compared to bottom heating, which coincides with the results we found for the evaporation process at 90 bar pressure.

### **Parabolic heat flux profile with parabolic firing**

In accordance with the high pressure studies, we continue the flux distribution studies for low pressure evaporator according to a parabolic profile. We see a couple of pressure/enthalpy slugs in figure (25) and after approximately 117 [s] simulation, the pressure rises rapidly. The fluid is here in a saturated condition in which the saturation temperature increases only slightly as function of the pressure rise. Subsequently, the pressure drops back to the original level, and the temperature follows back down to the original level as well, until the enthalpy suddenly rises rapidly above the level from before. Here we experience a kind of flashing, where the fluid is changing state from saturated steam to superheated steam, with significant temperature increases to follow (+15 [°C]). In this context, the fluid velocity increases violently, locally up to 20 [m / s] within seconds. These slugs die gradually as time passes, and the flow stabilizes in a static situation after about 200 [s] of simulation.

### **Comparison of the flux profiles in low pressure evaporator**

In general, we can see that reduced sub-cooling provides a more smooth solution over time, without the strong pressure oscillations initiated from the two-phase transition point. This is despite that the density jump is even more pronounced at lower pressure. But the degree of sub-cooling and thus the lower compressibility of water than steam is enough to change this. The start-up process with different heat flux profiles causes different pressure distribution. In figure (36) for station A, one can observe a different pressure build-up, in terms of both time and place. The greatest pressure wave build-up in the evaporator occurs in the bottom firing scenario, and

this occurs earlier compared to the other runs. The lowest pressure build-up occurs ultimately at top firing and arrives later. At station B, there is no significant difference in the pressure observations. At station B, we can also see that the enthalpy fluctuations occur earlier and more frequently at the bottom firing than the other scenarios; see figure (37). There are very significant differences in density for the bottom firing at station A. Here there is a lower density level created, significantly, earlier in the simulation, supplied with a clear pulsation, but without exceeding the density level of the other three flux configurations. The same trend is reflected in the fluid temperature, which is illustrated in figure (38). Here we also assume a higher value for the bottom firing, supplied with early pulsations to follow. This phenomenon can affect the delicate metal structures of the tubing, which are susceptible to fatigue fractures. The material temperature is illustrated in figure (39), here shown as an average temperature of the tube wall. At station A, we can see a significantly higher material temperature (+3 [°C]) for the bottom-firing scenario, compared to the other scenarios. At station B, this is not applicable before we pass the two-phase region and move into the super-heat region.

### Comparison of high versus low-pressure evaporator

The evaporator at AVV2 is almost identical to that of SKV3. DONG Energy - Thermal Power has carried out experiments with reduced evaporator pressure at AVV2, where outlet pressure was reduced from 90 [bar] to 56 [bar] and minimum flow was 86 [kg/s]. This did not cause any major drama, even though the boiler manufacturer has assigned a minimum pressure of 90 [bar]. When we compare the two simulations carried out at 90 [bar] and 56 [bar], respectively, we notice that the high-pressure case has higher sub-cooling of the fluid (inlet enthalpy common for both cases). The homogeneous model considers the sub-cooled liquid as almost incompressible, which leads to rapid pressure oscillations in the sub-cooled sector of the evaporator, and when the fluid is transferred to the two-phase region, the density dramatically decreases with pressure oscillations to follow. In the case of low-pressure evaporation, we have a moderate sub-cooling of the fluid, but conversely an even more withdrawn reduction

of density, when passing the two-phase region. This initiates violent pressure oscillations, which die out after approximately 100 [s]; see figure (26). It is worth noting that shortly after the start of firing, a peak occurs in the mass flux. The peak is highest for high-pressure evaporation with approximately 4250 [kg/m<sup>2</sup>s] after approximately 72 [s], while the low-pressure evaporation peaks earlier after only 25 [s] with a maximum mass flux of 2900 [kg/m<sup>2</sup>s]; see figure (28). One can observe more violent pressure and enthalpy fluctuations for low-pressure evaporation; see figures (26) and (27). Pressure oscillations are more common downstream of the evaporator; while at upstream station A, more quiet pressure conditions appear, which apparently do not affect the mal-distribution to the panel walls.

### CONCLUSION

In this paper, we use the fifth-order WENO solver to simulate the dynamic response of evaporator tubes corresponding to SKV3. Initially we describe the calibration process for the evaporator model, based on measurements from a steady state load case from SKV3 (sample 4) in table (2). The application is usable for various purposes, and initially we analyse four different heat flux distributions on the evaporator tube. We can observe several interesting dynamic phenomena that can be related to density-wave oscillations, we can see that bottom firing clearly reinforces the occurrence of density-waves, especially in the upstream section of the pipe (station A), where we can notice significant oscillations. There is a coupling between the density and the fluid velocity through the continuity equation. At certain periods, the fluid velocity is very low (read near-zero flow) and this can cause a significant temperature rise in the inner layer of the tube material. This again can increase the thermal load on the pipe wall, but we cannot trace any radial wall temperature increase in the simulation, because of the small time constants and because we are calculating an averaged tube wall temperature. The inner heat transfer will be weakened considerably when the flow rate approaches zero.

Another phenomenon which can be observed, is that the fluid temperature downstream is generally higher for the bottom firing scenario and there are temperature fluctuations of moderate strength.

Furthermore, the development of a pressure front occurs quickly in the bottom firing scenario, which gradually weakens, when the flow approaches a static state condition. During the transient period before steady state conditions are achieved, pressure oscillations occur. The remarkable thing is that the top firing scenario leads to surprising violent thermal fluctuations in fluid temperature, something that cannot be measured under operation of a plant. Conversely, we see that the top firing gives a more stable evaporator, in the sense that the evaporator has a lower degree of fluctuations in pressure and fluid velocity in the sub-cooled region, leading to a more safe operation of the evaporator during start-up. The applied load gradients are large, compared to the maximum allowable gradients on SKV3 (+/-8 MW/min.); see [5]. Further more, the restrictions compared to reduced lifetime of thick-walled components, like junction boxes or valves, are not taken into account in this analysis. We have now developed a tool that can be used in further studies of the evaporator stability, and we must of course ensure compliance with the evaporator design rules, especially rules related to the flow distribution to panel walls via junction boxes. Here significant sub-cooling is usually used in order to ensure a satisfactory distribution of a single-phase fluid to the evaporator wall.

## REFERENCES

- [1] Helmut Effenberger. *Dampferzeugung*. ISBN 3-540-64175-0 Springer-Verlage, Berlin 2000.
- [2] Christoph C. Richter. *Proposal of New Object-Oriented Equation-Based Model Libraries for Thermodynamic Systems*. Von der Fakultät für Maschinenbau, der Technischen Universität Carolo-Wilhelmina zu Braunschweig.
- [3] Anonymous. *Danmarks Energifremskrivning (October 2012)*. Edition, no.11, Energistyrelsen, ISBN: 978-87-7844-941-2, 2012.
- [4] Rehman S. *Solar radiation over Saudi Arabia and comparisons with empirical models*. Energy 1998;23(12):1077-1082.
- [5] Axel Ohrt Johansen. *Numerical study of evaporators in power plants for improved dynamic flexibility*. Ph.D thesis, Technical University Denmark, Department of Mechanical Engineering, 2013.
- [6] S. M. Ghiaasiaan. *Two-Phase Flow, Boiling, and Condensation in Conventional and Miniature Systems*, 1st Edition, Cambridge University Press, Georgia Institute of Technology, 2008.
- [7] H. Herman *VDI-Wärmeatlas* 9th Edition, Springer 2002, Berlin Heidelberg.
- [8] Pan, J. and Dong, Y and Yu, H and Bi, Q. and Hua, H. and Gao, F. and Yang, Z. *Mathematical modeling and thermo-hydraulic analysis of vertical water wall in an ultra supercritical boiler*, Applied Thermal Engineering vol. 29, 2009, p. 2500-2507.
- [9] Harald Griem *Untersuchung zur Thermohydraulik innenberippter Verdampferohre*, PhD thesis 1995, Technische Universität München, Lehrstuhl für Termische Kraftanlagen.
- [10] Anonymous. *Guarantee test results of steam turbine SVS3 - 98550369-KPG/TCM 99-6907 Confidential*, KEMA, Arnhem The Netherlands, 25 January 1999.
- [11] H. Schmidt, W. Köhler and W. Kastner. *"High-Pressure Test Facility - 25 Years of Operation, Framatome ANP GmbH"*. VGB Power Tech. 2001 p. 25-31.
- [12] Joachim Franke. *Untersuchung der hydrodynamischen Stabilität*. Von fachbereich Maschinenbau an der Technischen Hochschule Darmstadt zur Erlangung des Grades eines Doktor-Ingenieurs (Dr.-Ing.) genehmigte Dissertation vorgelegt von Dipl.-Phys. Joachim Franke aus Breslau. 1986, vol.1.
- [13] Pan, J. and Yang, D. and Dong, Z. and Zhu, T and Bi, Q, *Experimental investigation on heat transfer characteristics of low mass flux rifled tube upward flow*. International Journal of Heat and Mass Transfer 2011, vol. 54 p.2952-2961.
- [14] Yang, D., Pan, J., Zhou, C., Zhu, X., Bi, Q. and Chen, T. *Experimental investigation on heat transfer and frictional characteristics of vertical upward rifled tube in supercritical CFB*

- boiler*. Experimental Thermal and Fluid Science. 2011, vol 11 p.291-300.
- [15] Zhu, X. and Bi, Q. and Su, Q. and Yang, D. and Wang, J. and Wu, G. and Yu, S. *Self-compensating characteristic of steam-water mixture at low mass velocity in vertical upward parallel internally ribbed tubes*. Applied Thermal Engineering 2010 vol. 30, p. 2370-2377.
- [16] Fan, X. and Wu, S. *Heat transfer and frictional characteristics of rifled tube in a 1000 MW supercritical lignite-fired boiler*. 2010, p. 1-5. School of Energy Science and Engineering, Harbin Institute of Technology, China.
- [17] A.E. Bergles and J.H. Lienhard, et al. *Boiling and evaporation in small diameter channels*, Heat Transf. Eng.24 (2003) 18-40.
- [18] S. Kakac, B. Bon. *A review of two-phase flow dynamic instabilities in tube boiling system*, Int. J. Heat Mass Transfer 51 (2008) 399-433.
- [19] Capdeville,G.A *central WENO scheme for solving hyperbolic conservation laws on non-uniform meshes*, J. Comp. Phys., 2008, p. 2977-3014, vol. 4, num. 227.
- [20] Castro, Marcos. and Costa, Bruno. and Don, Wai Sun *High order weighted essentially non-oscillatory WENO-Z schemes for hyperbolic conservation laws*, Journal of Computational Physics, 2010, p. 1766-1792, number230.
- [21] Levy, D. and Pupo, G. and Russo, G. *Compact central WENO schemes for multidimensional conservation*, SIAM J. Sci. Comput. 2000, p. 656-672, vol.22.
- [22] Kurganov, Alexander and Tadmor, Eitan *New high-resolution central schemes for nonlinear conservation laws and convection-diffusion equations*, J. Comput. Phys. 2000, p. 241-282, vol.160.
- [23] Kurganov, A. and Levy, D. *A third-order semidiscrete central scheme for conservation laws and convection-diffusion equations*, SIAM J. Sci. Comp. 2000, p. 1461-1488, vol. 4, num. 22.
- [24] Gotlieb, S and Shu, C.W. *Total variation diminishing Runge-Kutta schemes* Math. Comp. 1998, p. 73-85 num. 67.
- [25] Bentz, P. Dale and Prasad, Kuldeep, R. *Thermal Performance of Fire Resistive Materials I. Characterization with Respect to Thermal performance Models*. NIST, Building and Fire research Laboratory, Gaithersburg, 2007, MD 20899-8615.
- [26] Anonymous. *Rohre aus warmfesten und hochwarmfesten Stählen Werkstoffblätter*, MannesMann Rohrenwerke, 1988, 1. ed.
- [27] F. Brandt. *FDBR-FACHBUCHREIHE Wärmeübertragung in Dampferzeugern und Wärmeaustauschern*, Vulkan-Verlag, Essen. 1985, BAND 2, FDBR FACHVERBAND DAMPFKESSEL, BEHÄLTER UND ROHRLEITUNGSBAU E. V., ISBN 3-8027-2274-4.

## APPENDIX

### NUMERICAL SOLUTION OF HYPERBOLIC TRANSPORT EQUATION

Let us consider a hyperbolic *system of balance laws* (SBL) formulated on a compact vector notation, given by equation (21), where  $\Phi$  is the unknown  $m$ -dimensional vector function,  $\mathbf{f}(\Phi)$  the flux vector,  $\mathbf{g}(\Phi)$  a continuous source vector function on the right hand side (RHS), with  $z$  as the single spatial coordinate and  $t$  the temporal coordinate,  $\Omega$  is partitioned in  $n_z$  non-overlapping cells:  $\Omega = \cup_{i=1}^{n_z} I_i \in [0, l_z]$ , where  $l_z$  is a physical length scale in the spatial direction. This system covers the general transport and diffusion equations used in many physical aspects and gas dynamics as well. The SBL system is subjected to the initial condition:

$$\Phi(z, 0) = \Phi_0(z) \quad (26)$$

and the below boundary conditions given by:

Dirichlet boundaries:

$$\begin{aligned} \Phi(z = 0, t) &= \Phi_A(t) \text{ and} \\ \Phi(z = l_z, t) &= \Phi_B(t) \end{aligned} \quad (27)$$

and

Neumann boundaries:

$$\begin{aligned} \frac{\partial \Phi(z = 0, t)}{\partial z} &= \frac{\partial \Phi_A(t)}{\partial z} \text{ and} \\ \frac{\partial \Phi(z = l_z, t)}{\partial z} &= \frac{\partial \Phi_B(t)}{\partial z} \end{aligned} \quad (28)$$

The above boundary conditions can be given by a combination of each type of boundaries. The Dirichlet condition is only specified, if we have ingoing flow conditions at the boundaries.

The development of a general numerical scheme for solving *PDE*'s may serve as universal finite-difference method, for solving non-linear convection-diffusion equations in the sense that they are not tied to the specific eigenstructure of a problem, and hence can be implemented in a straightforward manner as black-box solvers for general conservation laws and related equations, governing the spontaneous evolution of large gradient phenomena. The developed non-staggered grid is suitable for the modelling of transport of mass, momentum and energy and is illustrated in

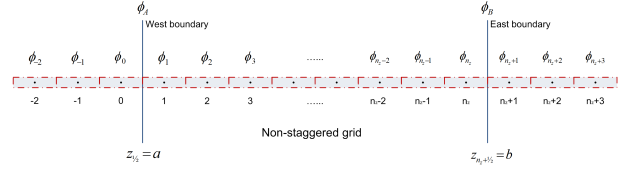


Figure 9: The computational grid  $[0, l_z]$  is extended to a set of ghost points for specifying boundary conditions.

figure (9), where the cell  $I_j = [z_{j-1/2}, z_{j+1/2}]$  has a cell width  $\Delta z$  and  $\Delta t$  the time step.

In this section, we review the central fifth order WENO schemes in one spatial dimension, developed by [19] with uses modified weight functions outlined by [20]. We recall the construction of the non-staggered central scheme for conservation laws. The starting point for the construction of the semi-discrete central-upwind scheme for equation (21) can be written in the following form:

$$\frac{d\Phi_j(t)}{dt} = -\frac{1}{\Delta z} [F_{j+1/2} - F_{j-1/2}] + S_j(\Phi). \quad (29)$$

where the numerical fluxes  $F_{j+1/2}$  are given by

$$F_{j+1/2} = \frac{a_{j+1/2}^+ f(\Phi_{j+1/2}^-) - a_{j+1/2}^- f(\Phi_{j+1/2}^+)}{a_{j+1/2}^+ - a_{j+1/2}^-} \quad (30)$$

$$+ \frac{a_{j+1/2}^+ a_{j+1/2}^-}{a_{j+1/2}^+ - a_{j+1/2}^-} [\Phi_{j+1/2}^+ - \Phi_{j+1/2}^-].$$

Notice that the accuracy of this scheme is determined by the accuracy of the reconstruction of  $\Phi$  and the ODE solver. In this paper the numerical solutions of (29) is advanced in time by mean of third order TVD Runge-Kutta method described by [24]. The local speeds of propagation can be estimated by

$$a_{j+1/2}^+ = \max \left\{ \lambda_N \left( \frac{\partial f(\Phi_{j+1/2}^-)}{\partial \Phi} \right), \lambda_N \left( \frac{\partial f(\Phi_{j+1/2}^+)}{\partial \Phi} \right), 0 \right\}, \quad (31)$$

$$a_{j+1/2}^- = \min \left\{ \lambda_1 \left( \frac{\partial f(\Phi_{j+1/2}^-)}{\partial \Phi} \right), \lambda_1 \left( \frac{\partial f(\Phi_{j+1/2}^+)}{\partial \Phi} \right), 0 \right\}.$$

with  $\lambda_1 < \dots < \lambda_N$  being the eigenvalues of the Jacobian given by  $\mathbf{J} = \frac{\partial f(\Phi(z,t))}{\partial \Phi}$ . Here,  $\Phi_{j+1/2}^+ = p_{j+1}(z_{j+1/2})$ , and  $\Phi_{j+1/2}^- = p_j(z_{j+1/2})$  are the corresponding right and left values of the

piecewise polynomial interpolant  $\{p_j(z)\}$  at the cell interface  $z=z_{j+1/2}$ .

To derive an essentially non-oscillatory reconstruction (ENO), we need to define three supplementary polynomials ( $\tilde{\Phi}_1, \tilde{\Phi}_2, \tilde{\Phi}_3$ ), approximating  $\Phi(z)$  with a lower accuracy on  $I_i$ . Thus, we define the polynomial of second-order accuracy,  $\tilde{\Phi}_1(z)$ , on the reduced stencil  $S_1: (I_{i-2}, I_{i-1}, I_i)$ ,  $\tilde{\Phi}_2(z)$  is defined on the stencil  $S_2: (I_{i-1}, I_i, I_{i+1})$ , whereas  $\tilde{\Phi}_3(z)$  is defined on the stencil  $S_3: (I_i, I_{i+1}, I_{i+2})$ . Now, we have to invert a  $3 \times 3$  linear system for the unknown coefficients  $\{a_j\}, j \in \{0, \dots, 2\}$ , defining  $\tilde{\Phi}_1, \tilde{\Phi}_2, \tilde{\Phi}_3$ . Once again, the constants determining the interpolation are pre-computed and stored before solving the PDEs. When the grid is uniform, the values of the coefficients for  $\tilde{\Phi}_1, \tilde{\Phi}_2$  and  $\tilde{\Phi}_3$  can be explicitly formulated. It is left to the reader to read [19] or [5] for further details about determining the coefficients in the reconstructed polynomials. To implement a specific solution technique, we extend the principle of the central WENO interpolation defined in [21]. First, we construct an ENO interpolant as a convex combination of polynomials that are based on different discrete stencils. Specifically, we define in the discrete cell  $I_i$ :

$$\tilde{\Phi}^i(z) \equiv \sum_j w_j \times \tilde{\Phi}_j(z), \quad (32)$$

$$\sum_j w_j = 1 \quad \text{for } w_j \geq 0 \quad \text{for } j \in \{1, \dots, 4\},$$

and  $\tilde{\Phi}_1, \tilde{\Phi}_2$  and  $\tilde{\Phi}_3$  are the previously defined polynomials.  $\tilde{\Phi}_4$  is the second-order polynomial defined on the central stencil  $S_5: (I_{i-2}, I_{i-1}, I_i, I_{i+1}, I_{i+2})$  and is calculated such that the convex combination in (32), will be fifth-order accurate in smooth regions. Therefore, it must verify:

$$\tilde{\Phi}_{opt}(z) = \sum_j C_j \times \tilde{\Phi}_j(z) \quad \forall z \in I_i, \quad (33)$$

$$\sum_j C_j = 1 \quad \text{for } C_j \geq 0 \quad \text{for } j \in \{1, \dots, 4\},$$

The calculation of  $\tilde{\Phi}_{i+1/2}^+, \tilde{\Phi}_{i+1/2}^-$  produces the fol-

lowing simplified result:

$$\begin{aligned} \tilde{\Phi}_{i+1/2}^+ &= \left(-\frac{7}{120}w_4 - \frac{1}{6}w_1\right)\tilde{\Phi}_{i-2} \\ &+ \left(\frac{1}{3}w_2 + \frac{5}{6}w_1 + \frac{21}{40}w_4\right)\tilde{\Phi}_{i-1} \\ &+ \left(\frac{5}{6}w_2 + \frac{1}{3}w_1 + \frac{11}{6}w_3 + \frac{73}{120}w_4\right)\tilde{\Phi}_i \\ &+ \left(-\frac{1}{6}w_2 - \frac{7}{6}w_3 - \frac{7}{120}w_4\right)\tilde{\Phi}_{i+1} \\ &+ \left(\frac{1}{3}w_3 - \frac{1}{60}w_4\right)\tilde{\Phi}_{i+2} \end{aligned} \quad (34)$$

$$\begin{aligned} \tilde{\Phi}_{i+1/2}^- &= \left(-\frac{1}{60}w_4 + \frac{1}{3}w_1\right)\tilde{\Phi}_{i-2} \\ &+ \left(-\frac{1}{6}w_2 - \frac{7}{6}w_1 - \frac{7}{120}w_4\right)\tilde{\Phi}_{i-1} \\ &+ \left(\frac{5}{6}w_2 + \frac{1}{3}w_3 + \frac{11}{6}w_1 + \frac{73}{120}w_4\right)\tilde{\Phi}_i \\ &+ \left(\frac{1}{3}w_2 - \frac{5}{6}w_3 + \frac{21}{40}w_4\right)\tilde{\Phi}_{i+1} \\ &+ \left(-\frac{1}{6}w_3 - \frac{7}{120}w_4\right)\tilde{\Phi}_{i+2} \end{aligned} \quad (35)$$

To calculate the weights  $w_j, j \in \{1, 2, 3, 4\}$ , we review another technique to improve the classical smoothness indicators to obtain weights that satisfy the sufficient conditions for optimal order of accuracy. It is well known from [19], that the original WENO is fifth order accurate for smooth parts of the solution domain except near sharp fronts and shocks. The idea here is taken from [20] and uses the hole five point stencil  $S_5$  to define a new smoothness indicator of higher order than the classical smoothness indicator  $IS_i$ . The general form of indicators of smoothness are defined in [21]:

$$IS_j^i = a_1^2 \Delta z^2 + \frac{13}{3} a_2^2 \Delta z^4 + O(\Delta z^6), \quad (36)$$

$$j \in \{1, 2, 3\}.$$

and the form of  $IS_4^i$  is given by [19]:

$$IS_4^i = a_1^2 \Delta z^2 + \left[ \frac{13}{3} a_2^2 + \frac{1}{2} a_1 a_3 \right] \Delta z^4 + O(\Delta z^6). \quad (37)$$

where  $a_0$  and  $a_1$  can be determined by solving the coefficients to reconstructed polynomial  $\tilde{\Phi}_4$  on  $S_5$ . For estimating the weights  $w_k, k \in \{1, 2, 3, 4\}$ , we proceed as follows: Define

$$IS_k^* = \frac{IS_k + \varepsilon}{IS_k + \varepsilon + \tau_5} \quad (38)$$

where  $IS_k$ ,  $k \in \{1, 2, 3\}$  are given by (36),  $IS_4$  given by (37) and  $\tau_5 = |IS_1 - IS_3|$ . The constant  $\varepsilon$  is a small number. In some articles  $\varepsilon \approx$  from  $1 \cdot 10^{-2}$  to  $1 \cdot 10^{-6}$ , see [21]. Here we use much smaller values of  $\varepsilon$  for the mapped and improved schemes in order to force this parameter to play only its original role of not allowing vanishing denominators at the weight definitions. The weights  $w_k$  are defined as:

$$w_k = \frac{\alpha_k^*}{\sum_{l=1}^4 \alpha_l^*}, \quad \alpha_k^* = \frac{C_k}{IS_k^*}, \quad k \in \{1, 2, 3, 4\} \quad (39)$$

The constants  $C_j$  represent ideal weights for (32). As already noted in [21], the freedom in selecting these constants has no influence on the properties of the numerical stencil; any symmetric choice in (33), provides the desired accuracy for  $\tilde{\Phi}_{opt}$ . In what follows, we make the choice as in [19]:

$$C_1 = C_3 = 1/8, C_2 = 1/4 \text{ and } C_4 = 1/2. \quad (40)$$

### Convection-Diffusion equations

Let us again consider the general System of Conservation Laws (SCL), given by equation (21), where the source term  $g$  is replaced by a dissipative flux:

$$\frac{\partial \Phi(z, t)}{\partial t} + \frac{\partial f(\Phi(z, t))}{\partial z} = \frac{\partial}{\partial z} \left( g(\Phi(z, t), \frac{\partial \Phi}{\partial z}) \right), \quad (41)$$

$$t \geq 0, \quad z \in \Omega$$

The gradient of  $g$  is formulated on the compressed form:  $g(\Phi, \frac{\partial \Phi}{\partial z})_z$  as a nonlinear function  $\neq$  zero. This term can degenerate (41) to a strongly parabolic equation, admitting non smooth solutions. To solve it numerically is a highly challenging problem. Our fifth-order semi-discrete scheme, (29)-(30), can be applied to (21) in a straightforward manner, since we can treat the hyperbolic and the parabolic parts of (41) simultaneously. This results in the following conservative scheme:

$$\frac{d\Phi_j(t)}{dt} = -\frac{1}{\Delta z} [F_{j+1/2} - F_{j-1/2}] + G_j(\Phi, t). \quad (42)$$

Here  $F_{j+1/2}$  is our numerical convection flux, given by equation (30) and  $G_j$  is a high-order approximation to the diffusion flux  $g(\Phi, \frac{\partial \Phi}{\partial z})_z$ . Similar to the case of the second-order semi-discrete scheme of

[22], operator splitting is not necessary for the diffusion term. By using a fourth order central differencing scheme, outlined by [23], we can apply our fifth-order semi-discrete scheme, given by (29) and (30), to the parabolic equation (21), where  $g(\Phi, \frac{\partial \Phi}{\partial z})_z$  is a function of  $\Phi$  and its derivative in space (diffusion). The diffusion term can be expressed by a high-order approximation:

$$G_j(t) = \frac{1}{12\Delta z} [-G(\Phi_{j+2}, (\Phi_z)_{j+2}) + 8 \cdot G(\Phi_{j+1}, (\Phi_z)_{j+1})] \\ - \frac{1}{12\Delta z} [8 \cdot G(\Phi_{j-1}, (\Phi_z)_{j-1}) + G(\Phi_{j-2}, (\Phi_z)_{j-2})] \quad (43)$$

where

$$(\Phi_z)_{j+2} = \frac{1}{12\Delta z} [25\Phi_{j+2} - 48\Phi_{j+1}] \\ + \frac{1}{12\Delta z} [36\Phi_j - 16\Phi_{j-1} + 3\Phi_{j-2}], \quad (44)$$

$$(\Phi_z)_{j+1} = \frac{1}{12\Delta z} [3\Phi_{j+2} + 10\Phi_{j+1}] \\ - \frac{1}{12\Delta z} [18\Phi_j + 6\Phi_{j-1} - \Phi_{j-2}], \quad (45)$$

$$(\Phi_z)_{j-1} = \frac{1}{12\Delta z} [\Phi_{j+2} - 6\Phi_{j+1}] \quad (46)$$

$$+ \frac{1}{12\Delta z} [18\Phi_j - 10\Phi_{j-1} - 3\Phi_{j-2}] \quad \text{and}$$

$$(\Phi_z)_{j-2} = \frac{1}{12\Delta z} [-3\Phi_{j+2} + 16\Phi_{j+1}] \\ - \frac{1}{12\Delta z} [36\Phi_j + 48\Phi_{j-1} - 25\Phi_{j-2}] \quad (47)$$

and  $\Phi_j$  are the point-values of the reconstructed polynomials.

### Source Term

Next, let us consider the general SCL given by (21) and restrict our analysis to the source term of the form:  $g(\Phi, t)$  as a continuous source vector function  $\neq$  zero. By integrating system (21) over a finite space-time control volume  $I_i, \Delta t$  one obtains a finite volume formulation for the system of balance laws, which usually takes the form

$$\Phi(z, t)_j^{n+1} = \Phi(z, t)_j^n - \frac{\Delta t}{\Delta z} (f_{j+1/2} - f_{j-1/2}) \quad (48) \\ + \Delta t g(z, t)_j, \quad t \geq 0, \quad z \in \Omega$$

The integration of (21) in space and time gives rise to a temporal integral of the flux across the element

boundaries  $f_{j+1/2}$  and to a space-time integral  $g_i$  of the source term inside  $I_i$ . In practice, one must replace the integrals of the flux and the source in (48) by some suitable approximations, that is to say one must choose a concrete numerical scheme. For SBL a numerical source must be chosen. Here, not only the three classical properties are required, but some additional properties are needed for the global numerical scheme: It should be well-balanced, i.e. able to preserve steady states numerically. It should be robust also on coarse grids if the source term is stiff.

### Boundary conditions for Non-staggered grid

For a system of  $m$  equations we need a total of  $m$  boundary conditions. Typically some conditions must be prescribed at the inlet boundary ( $z=a$ ) and some times at the outlet boundary ( $z=b$ ). How many are required at each boundary depends on the number of eigenvalues of the Jacobian  $\mathbf{A}$  that are positive and negative, respectively and whether the information is marching in or out for the boundaries.

By extending the computational domain to include a few additional cells on either end of the solution domain, called ghost cells, whose values are set at the beginning of each time step in some manner that depends on the boundary condition. In figure (9) is illustrated a grid with three ghost cells at each boundary. The idea behind the ghost point approach is to express the value of the solution at control points outside the computational domain in terms of the values inside the domain plus the specified boundary condition. This allows the boundary condition to be imposed by a simple modification of the internal coefficients using the coefficients of the fictitious external point. This can result in a weak imposition of the boundary condition, where the boundary flux not exactly agree with the boundary condition. By establishing a Taylor expansion around the boundary  $a$  or  $(b)$ , we can express a relationship between the ghost points outside the solution domain and grid points inside the domain. For further details see [5].

### Time discretization

The semi-discrete ODE given by (29) is a time dependent system, which can be solved by a TVD Runge-Kutta method presented by [24]. The optimal third order TVD Runge-Kutta method is given

by

$$\begin{aligned}\Phi_j^{(1)} &= \Phi_j^n + \Delta t L(\Phi_j^n), \\ \Phi_j^{(2)} &= \frac{3}{4}\Phi_j^n + \frac{1}{4}\Phi_j^{(1)} + \frac{1}{4}\Delta t L(\Phi_j^{(1)}), \\ \Phi_j^{n+1} &= \frac{1}{3}\Phi_j^n + \frac{2}{3}\Phi_j^{(2)} + \frac{2}{3}\Delta t L(\Phi_j^{(2)}), \text{ for } j \in [1, n_z].\end{aligned}\tag{49}$$

The stability condition for the above schemes is

$$CFL = \max \left( u_j^n \frac{\Delta t}{\Delta z} \right) \leq 1, \tag{50}$$

where CFL stands for the *Courant-Friedrichs-Lewy* condition and  $u_j^n$  is the maximum propagation speed in cell  $I_j$  at time level  $n$ .

## FIGURES

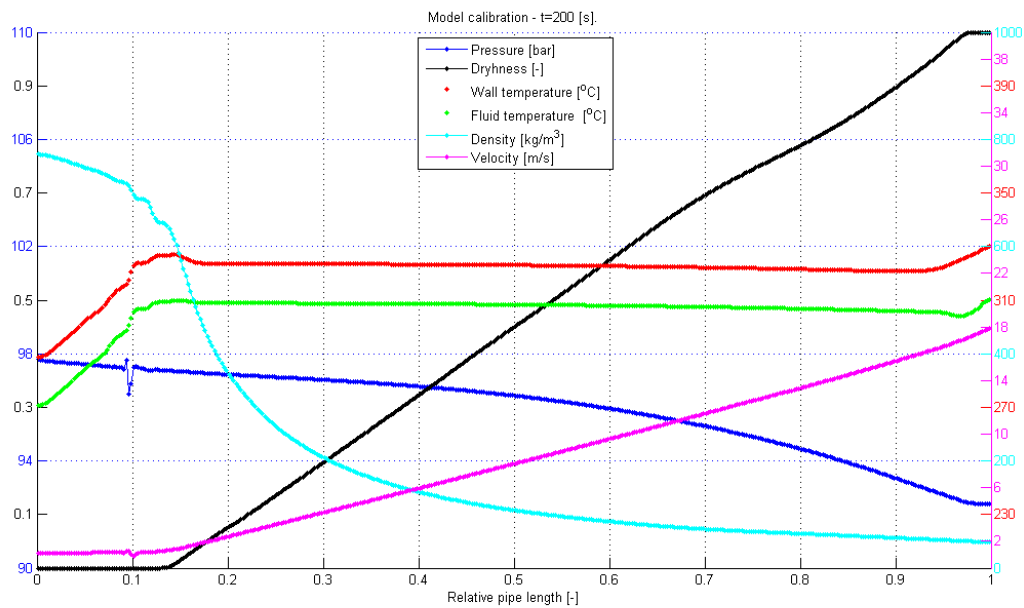


Figure 10: Line series of heat pipe calibration, t=200[s].

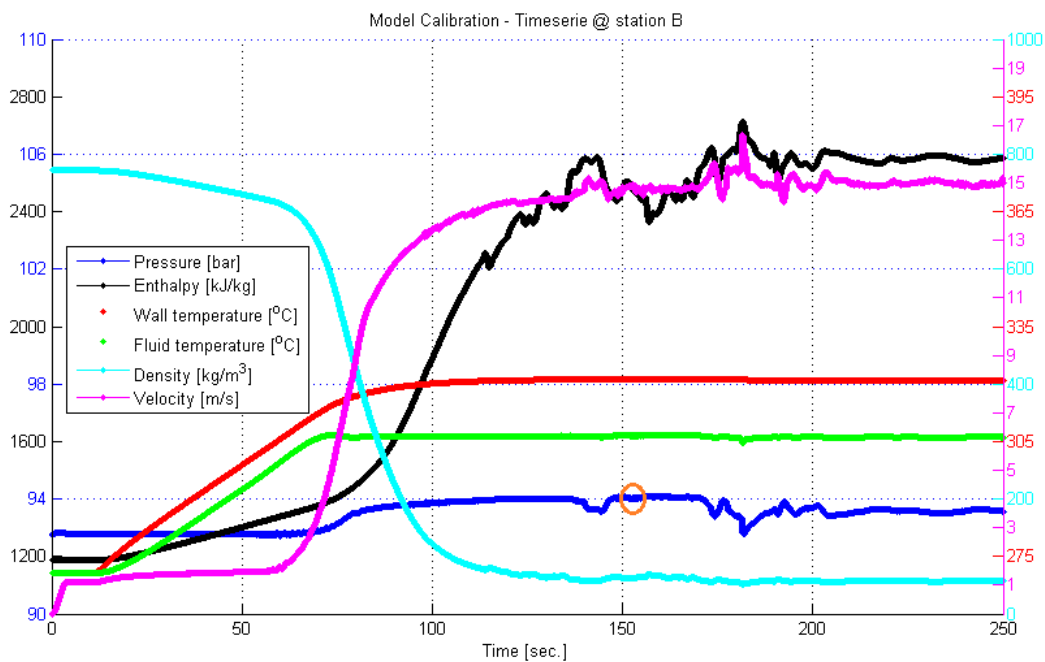


Figure 11: Time series of heat tube calibration, station B.

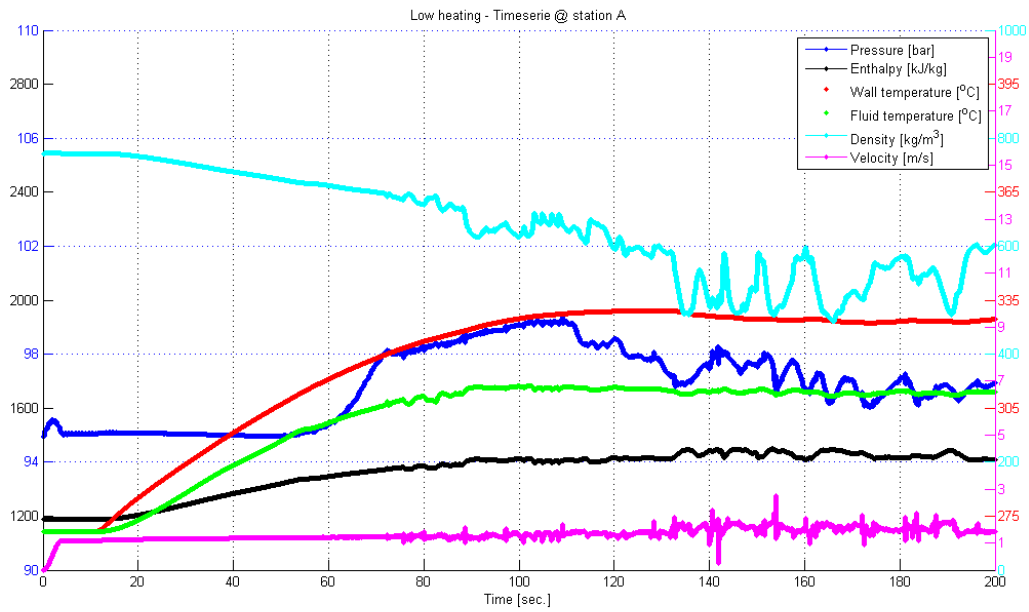


Figure 12: Time series of bottom firing in SKV3 evaporator model at station A.

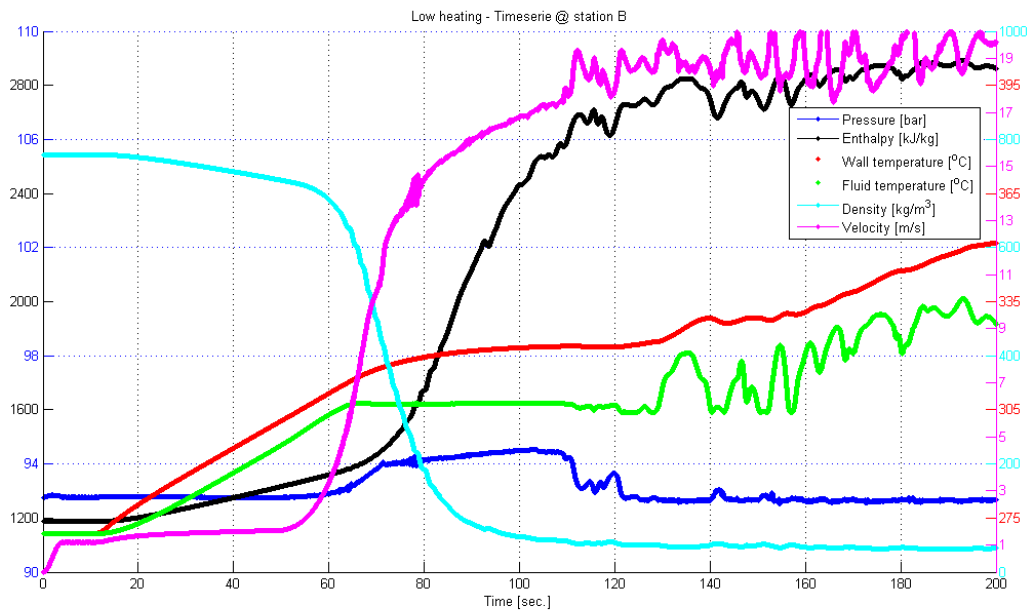


Figure 13: Time series of bottom firing in SKV3 evaporator model at station B.

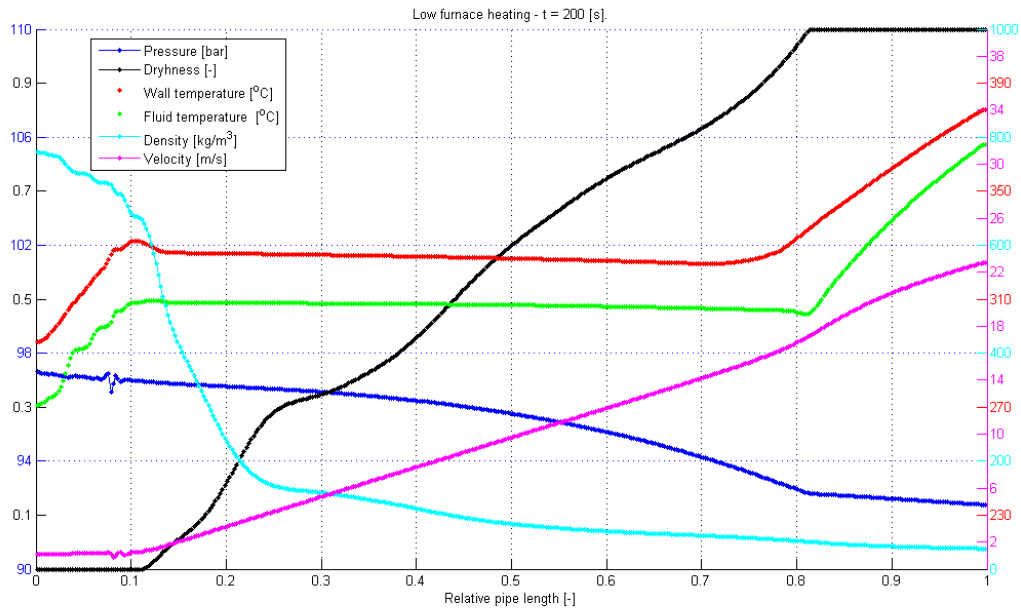


Figure 14: Bottom firing in SKV3 boiler, after 200 [s].

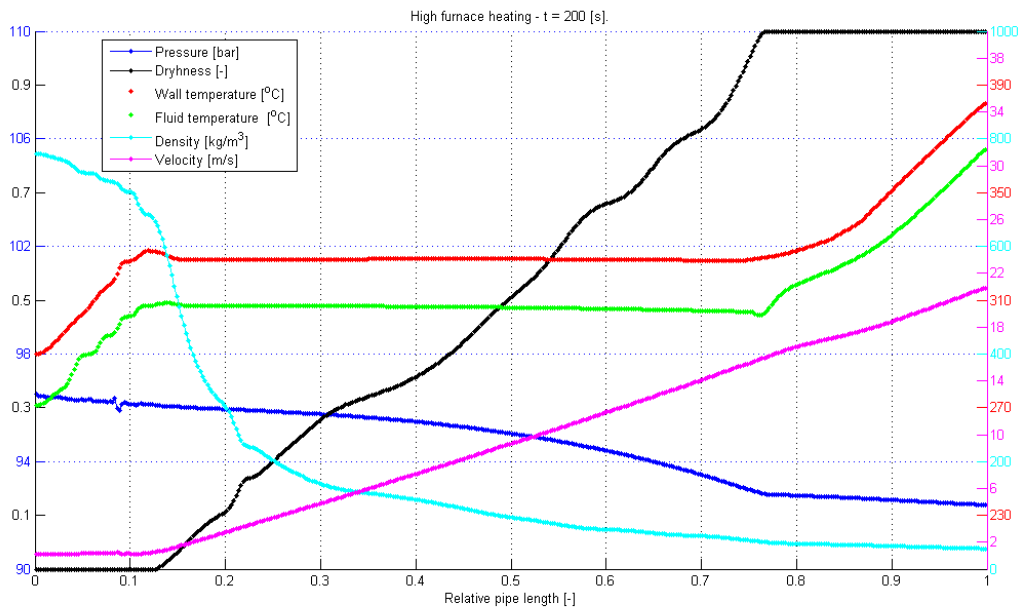


Figure 15: Top firing in SKV3 boiler, after 200 [s].

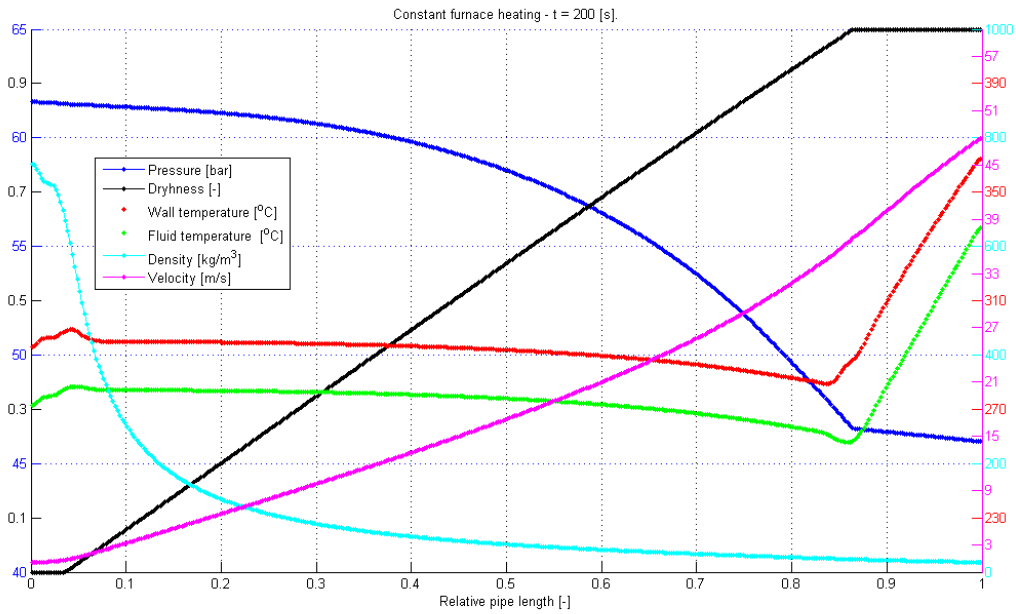


Figure 16: Constant heat flux to boiler, after 200 [s].

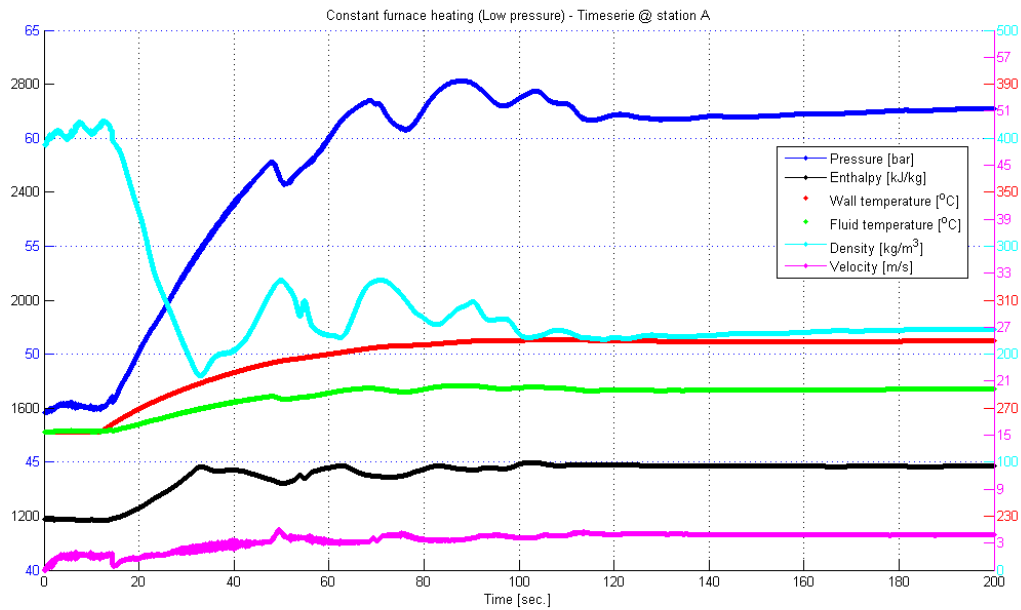


Figure 17: Time series of constant heat flux at the SKV3 evaporator model at station A.

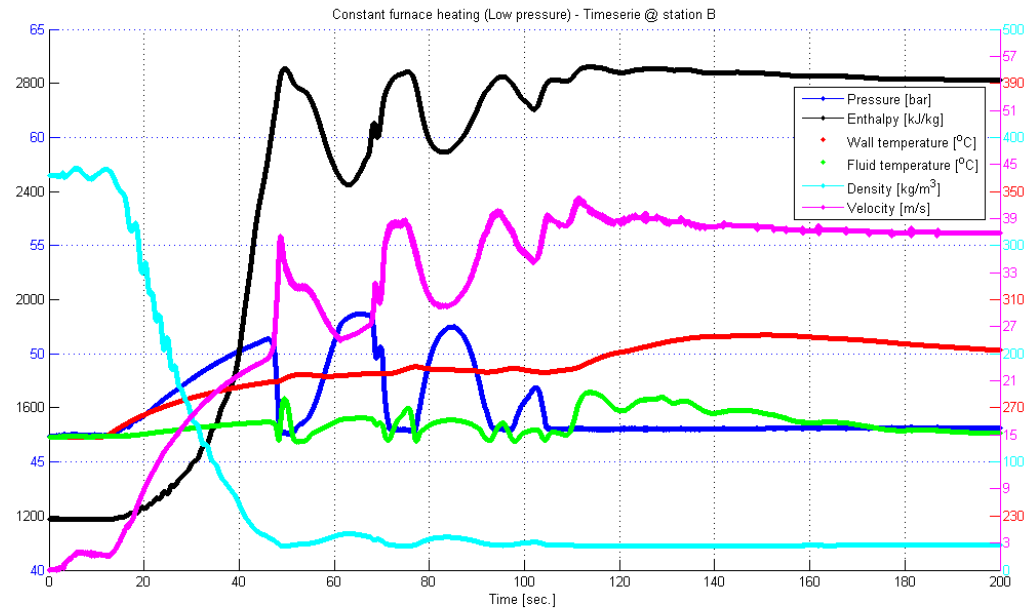


Figure 18: Time series of constant heat flux at the SKV3 evaporator model at station B.

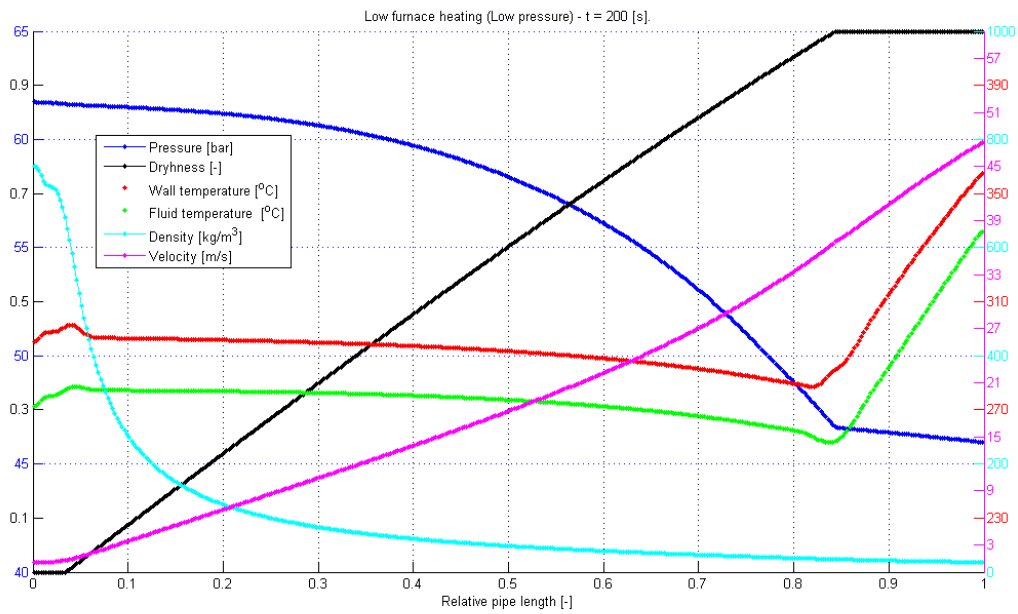


Figure 19: Bottom heating in the SKV3 boiler after 200 [s].

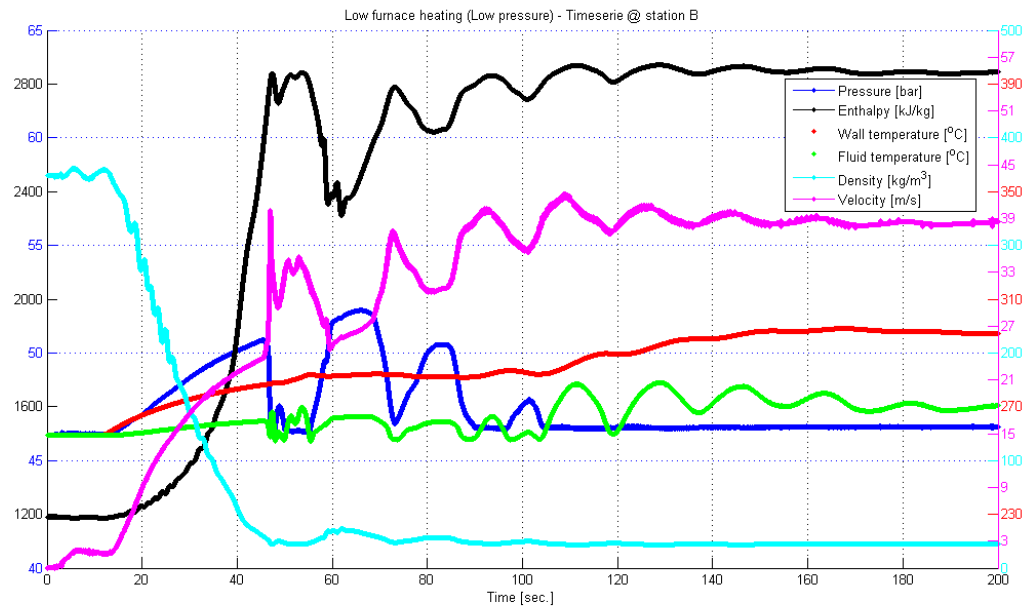


Figure 20: Time series of bottom heating in the SKV3 evaporator model at station B.

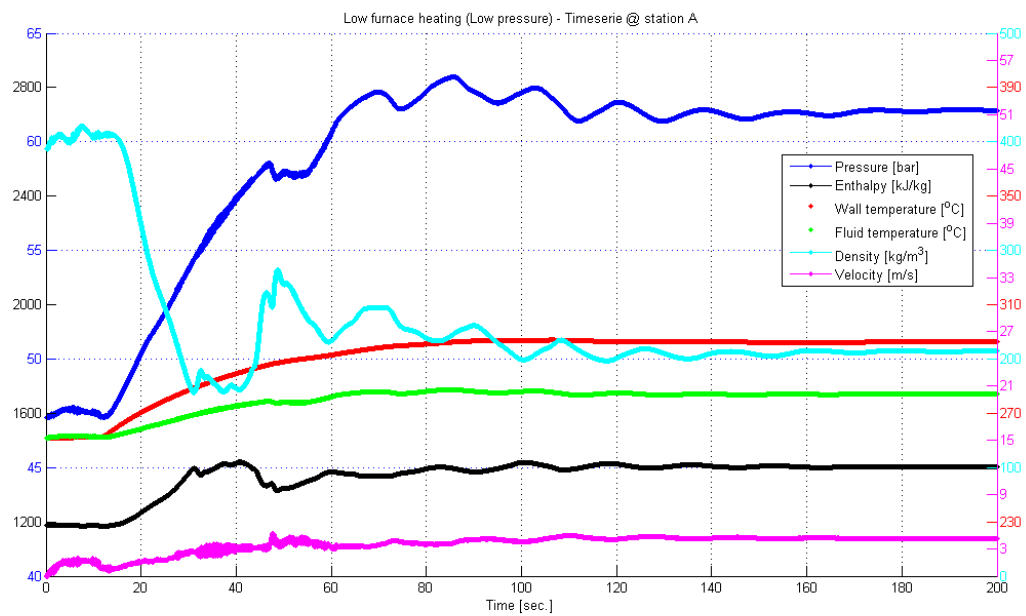


Figure 21: Time series of bottom heating in the SKV3 evaporator model at station A.

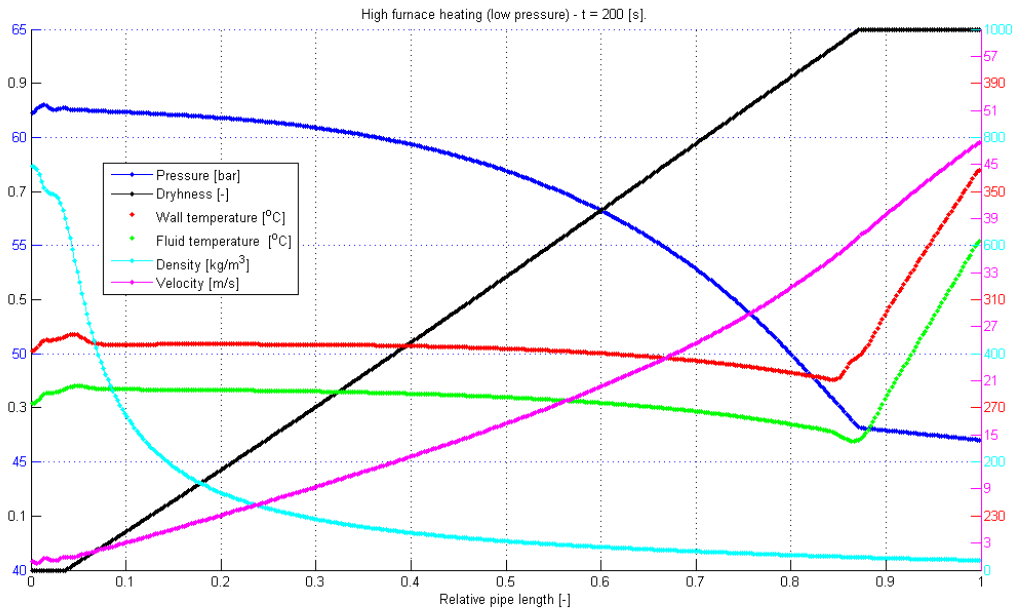


Figure 22: Top heating in the SKV3 boiler after 200 [s].

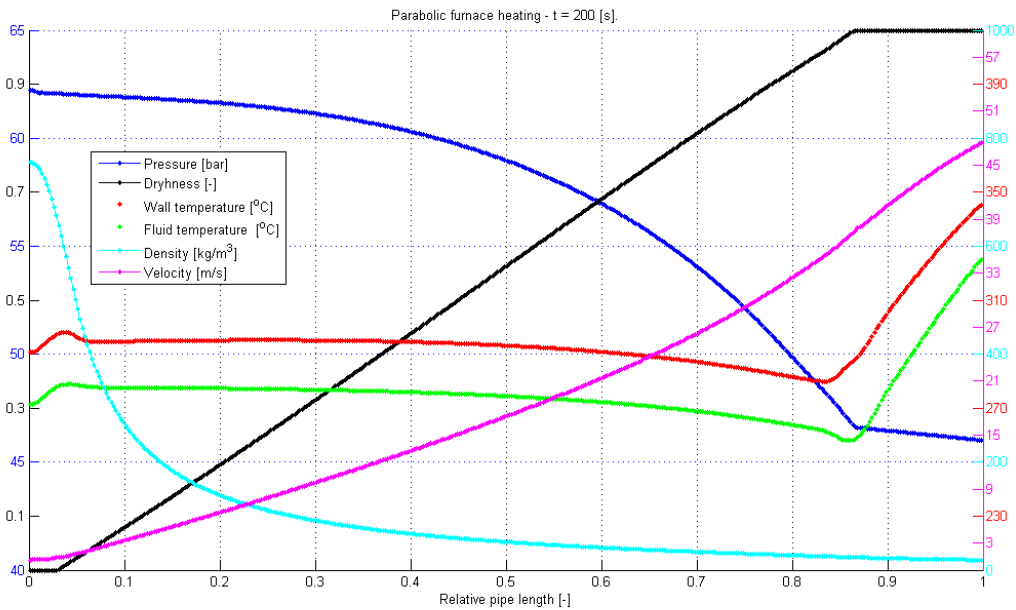


Figure 23: Parabolic heating in SKV3 boiler after 200 [s].

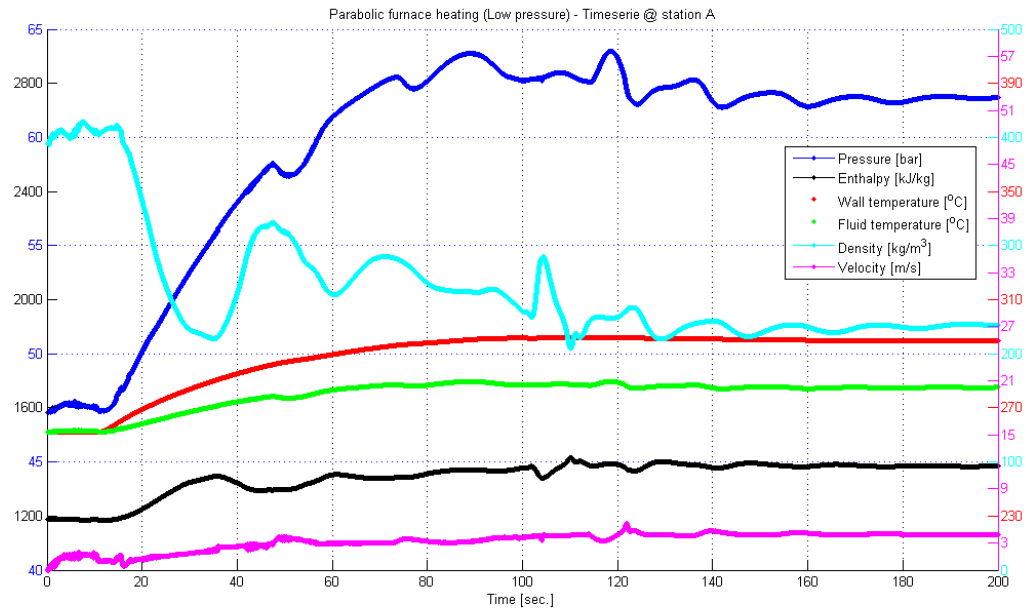


Figure 24: Time series of parabolic heating in SKV3 evaporator model at location A.

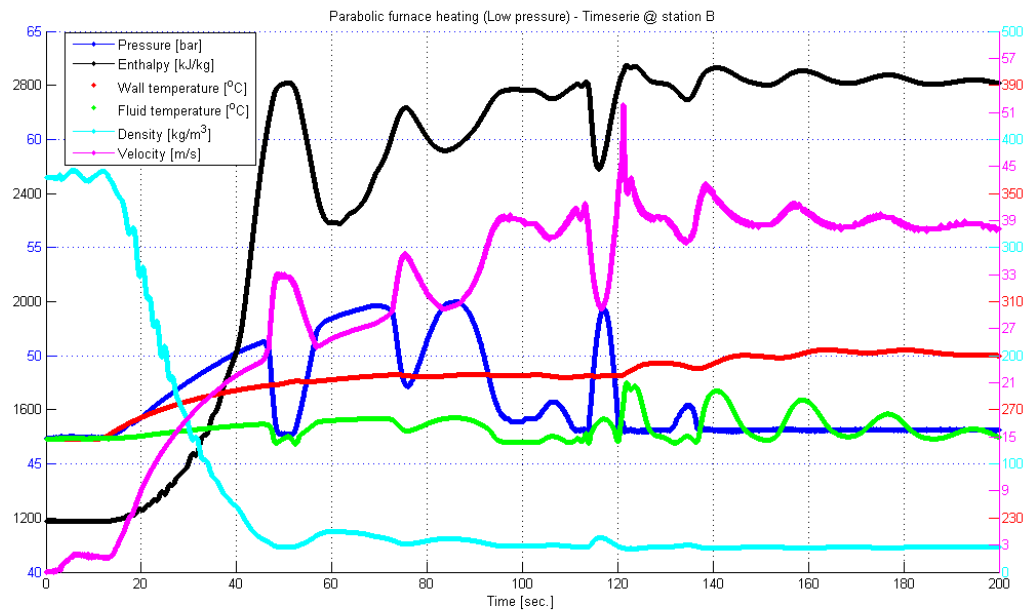


Figure 25: Time series of parabolic heating in SKV3 evaporator model at location B.

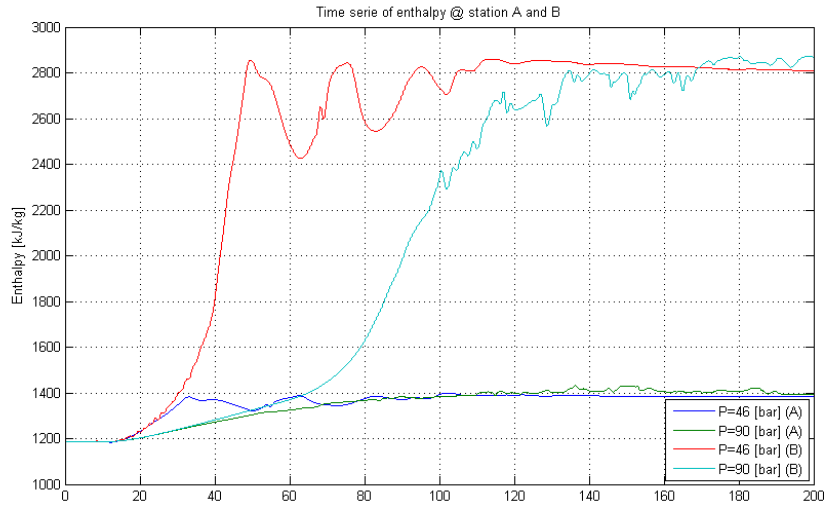


Figure 26: Comparison of enthalpy at different evaporation pressure at station A and B.

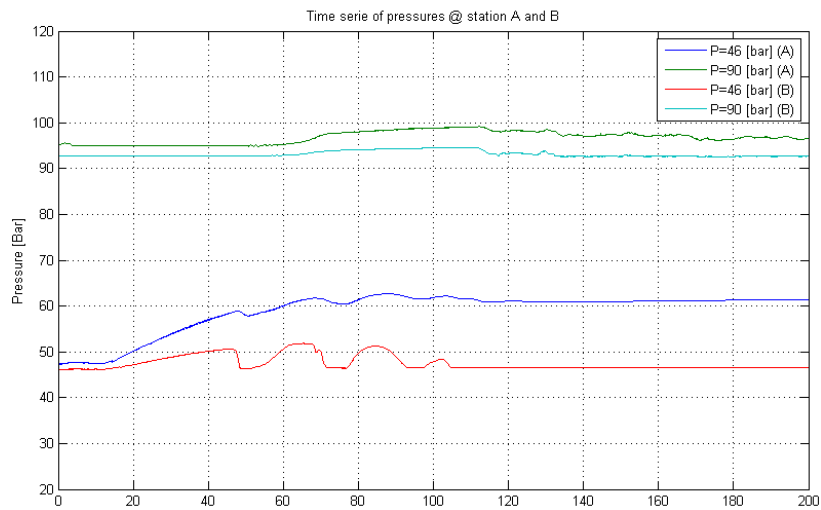


Figure 27: Comparison of pressure level at different evaporation pressure at station A and B.

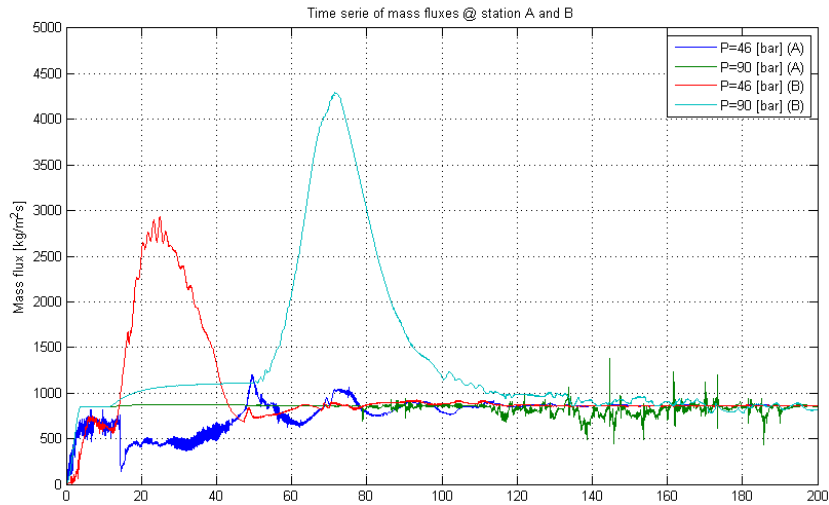


Figure 28: Comparison of mass flux at different evaporation pressure at station A and B.

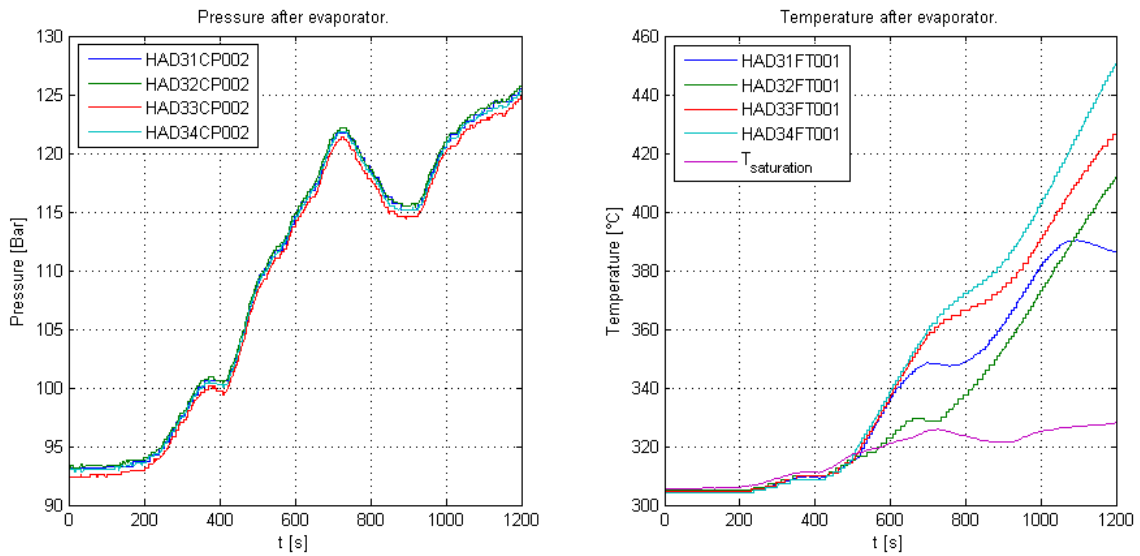


Figure 29: Pressure and temperature after boiler top section - sample 3.

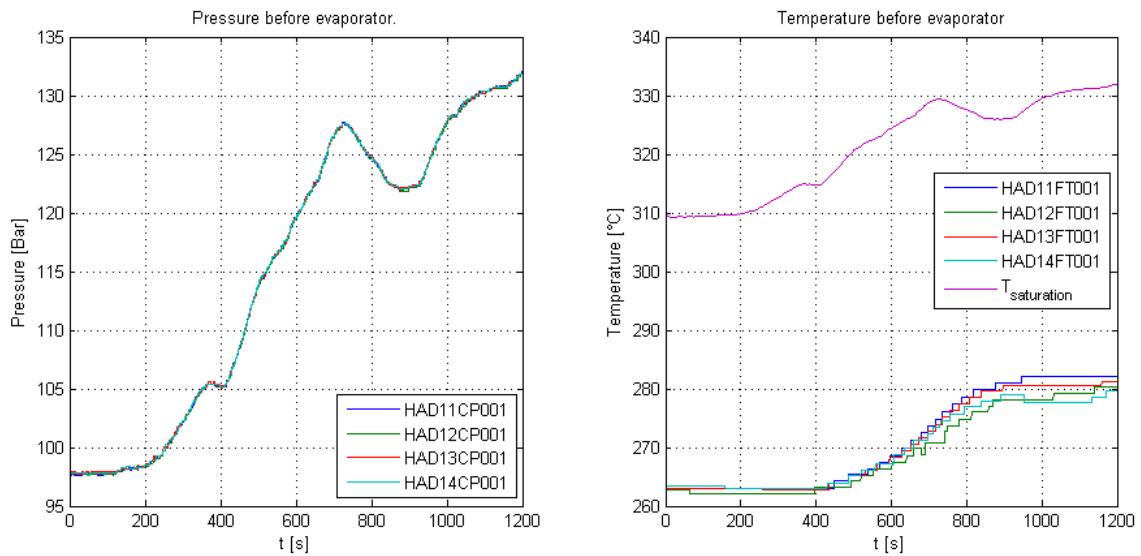


Figure 30: Pressure and temperature after ECO - sample 3.

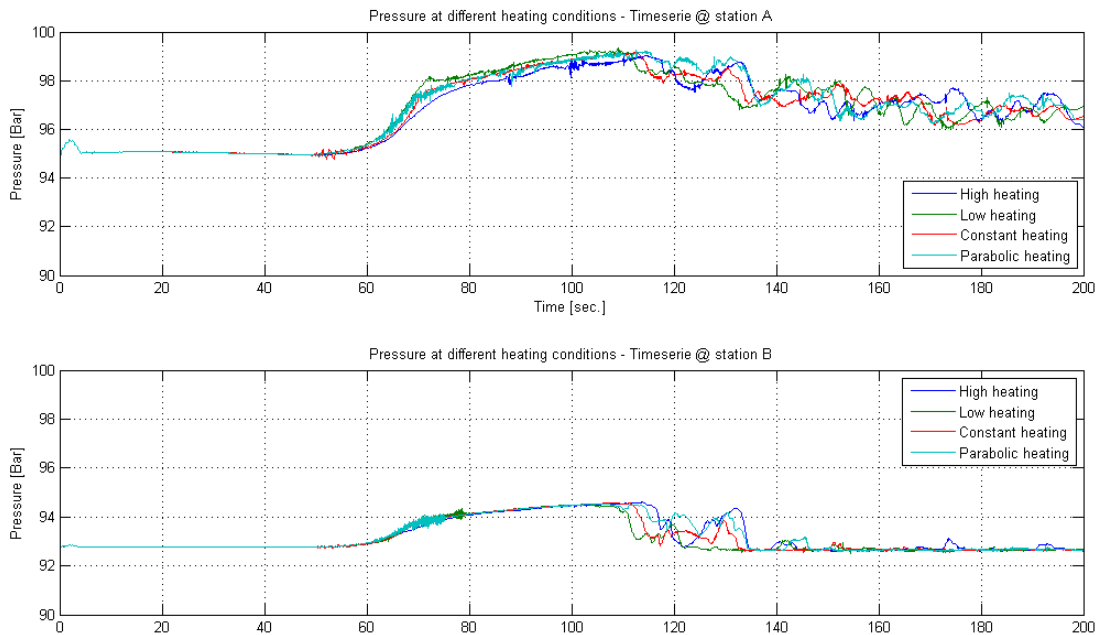


Figure 31: Comparison of the firing profiles on the SKV3 evaporator with respect to fluid pressure.

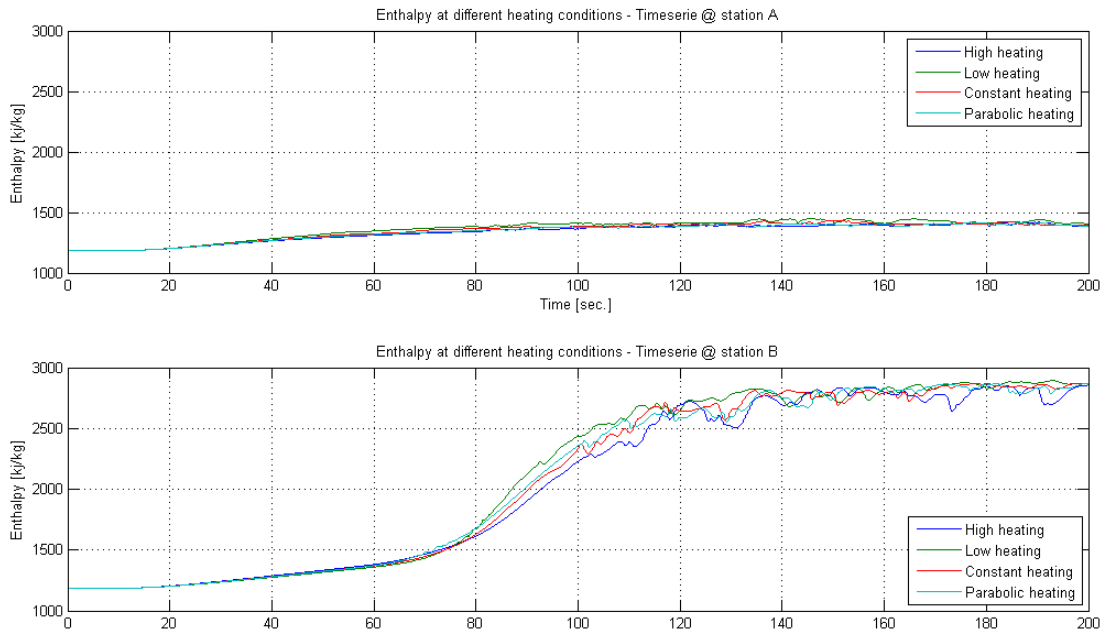


Figure 32: Comparison of the firing profiles on the SKV3 evaporator with respect to fluid enthalpy.

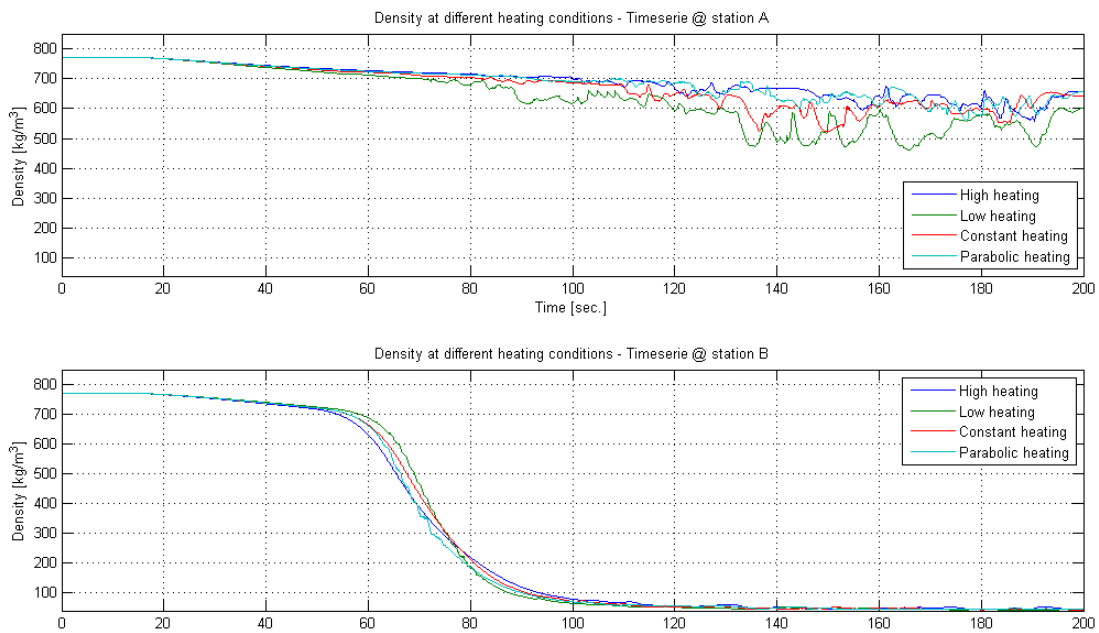


Figure 33: Comparison of the firing profiles on the SKV3 evaporator with respect to fluid density.

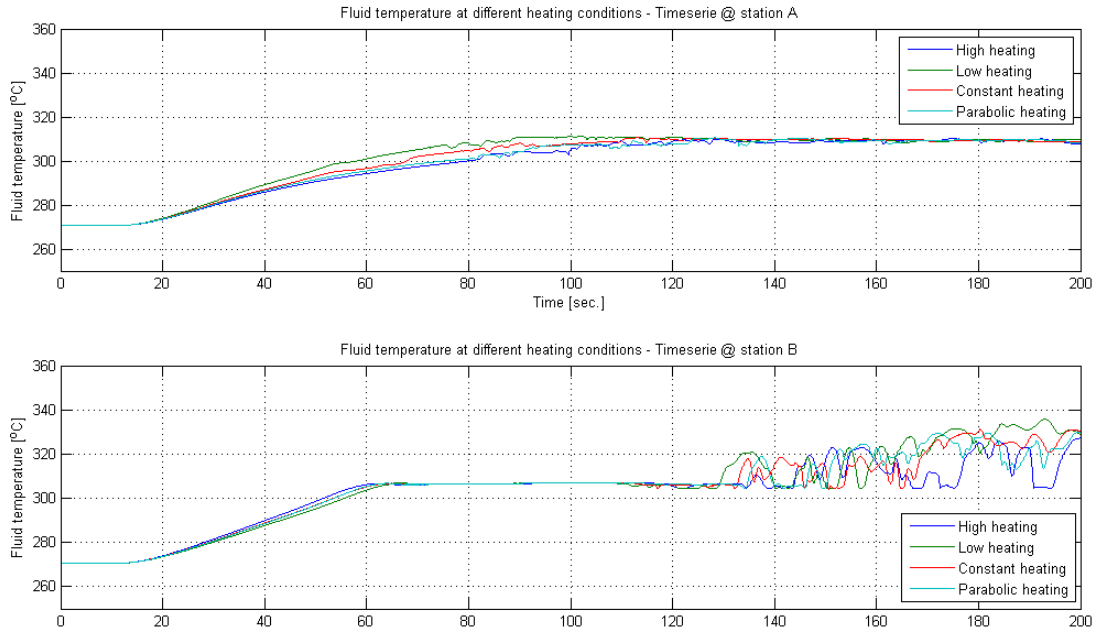


Figure 34: Comparison of the firing profiles on the SKV3 evaporator with respect to fluid temperature.

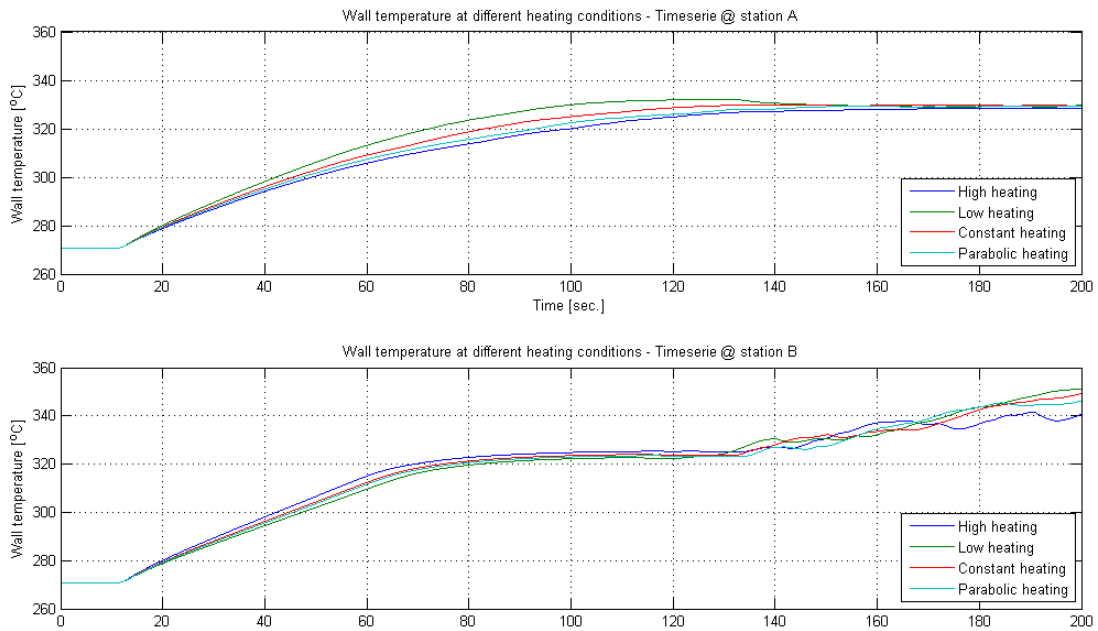


Figure 35: Comparison of the firing profiles on the SKV3 evaporator with respect to wall temperature.

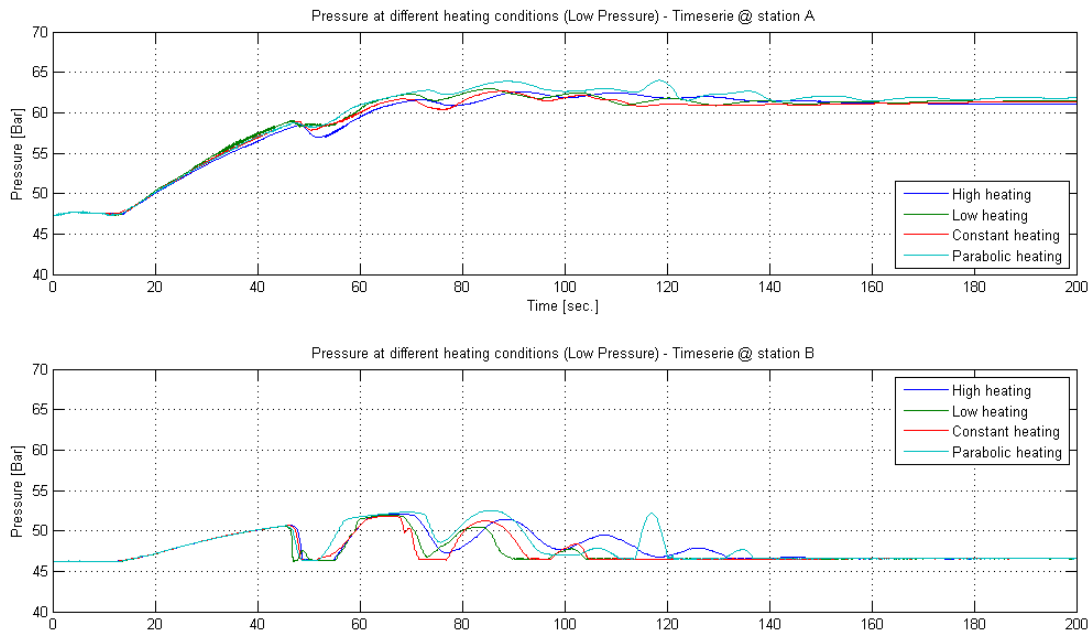


Figure 36: Comparison of the firing profiles on the SKV3 evaporator with respect to fluid pressure.

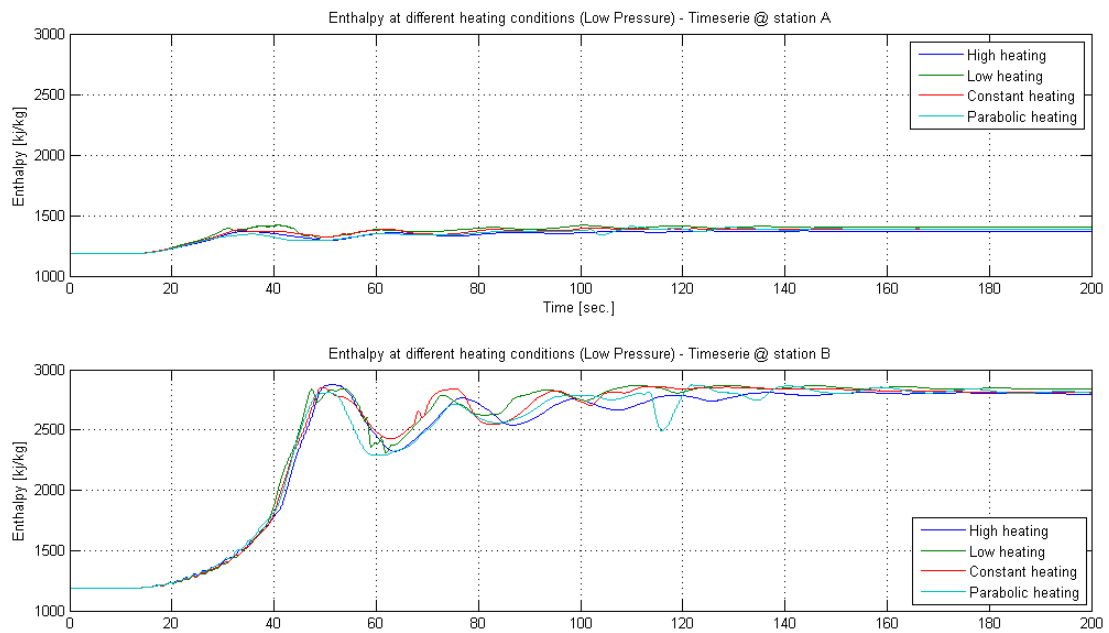


Figure 37: Comparison of the firing profiles on the SKV3 evaporator with respect to fluid enthalpy.

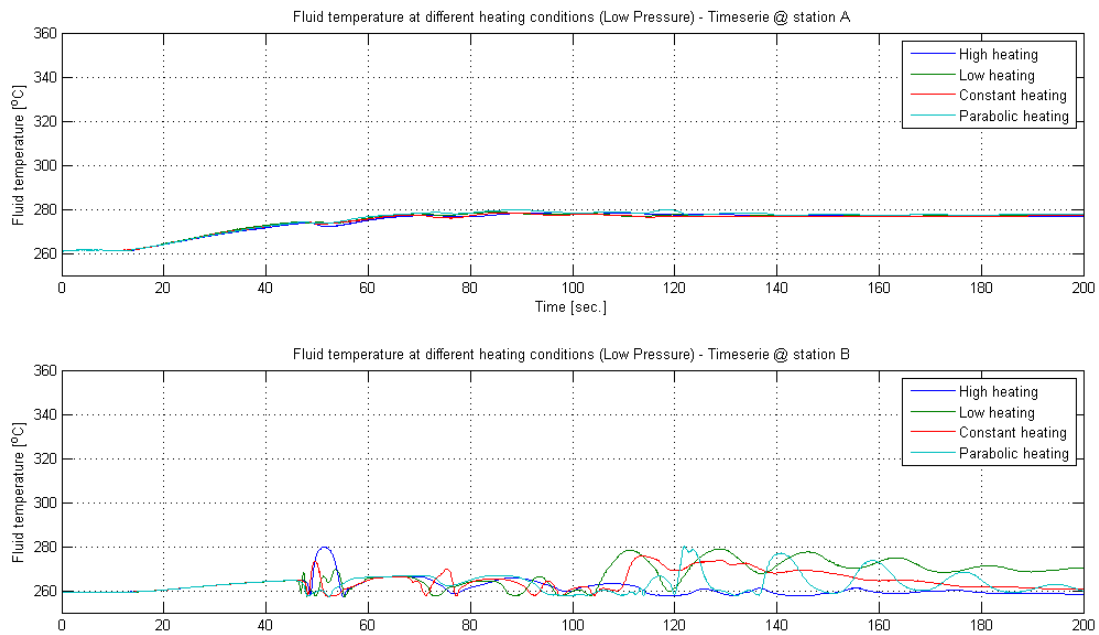


Figure 38: Comparison of the firing profiles on SKV3 evaporator with respect to fluid temperature at stations A and B.

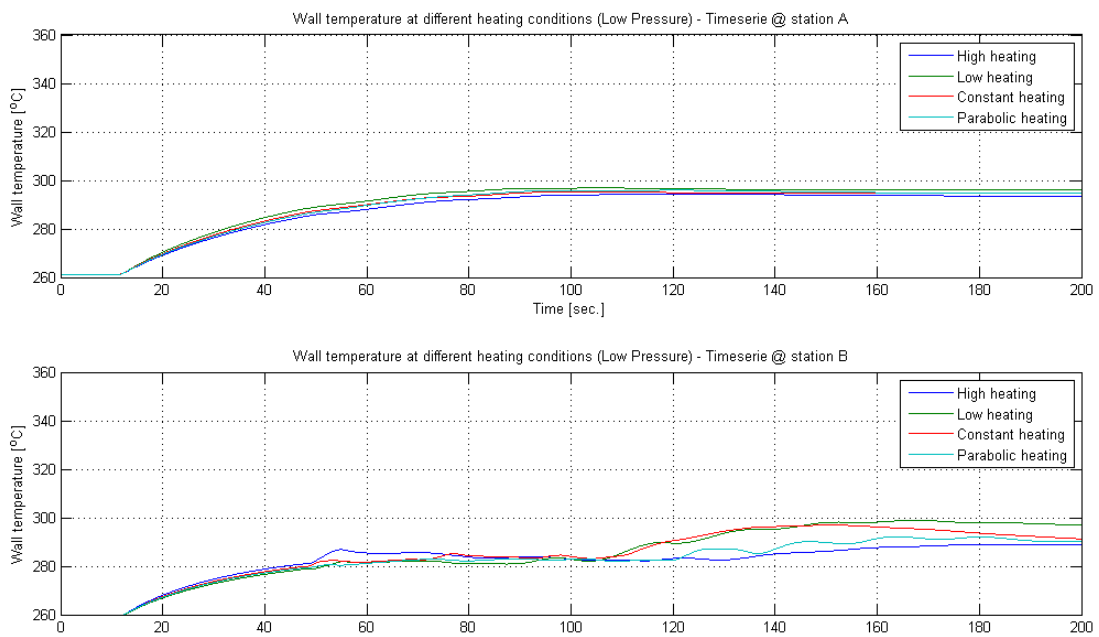


Figure 39: Comparison of the firing profiles on the SKV3 evaporator with respect to wall temperature.

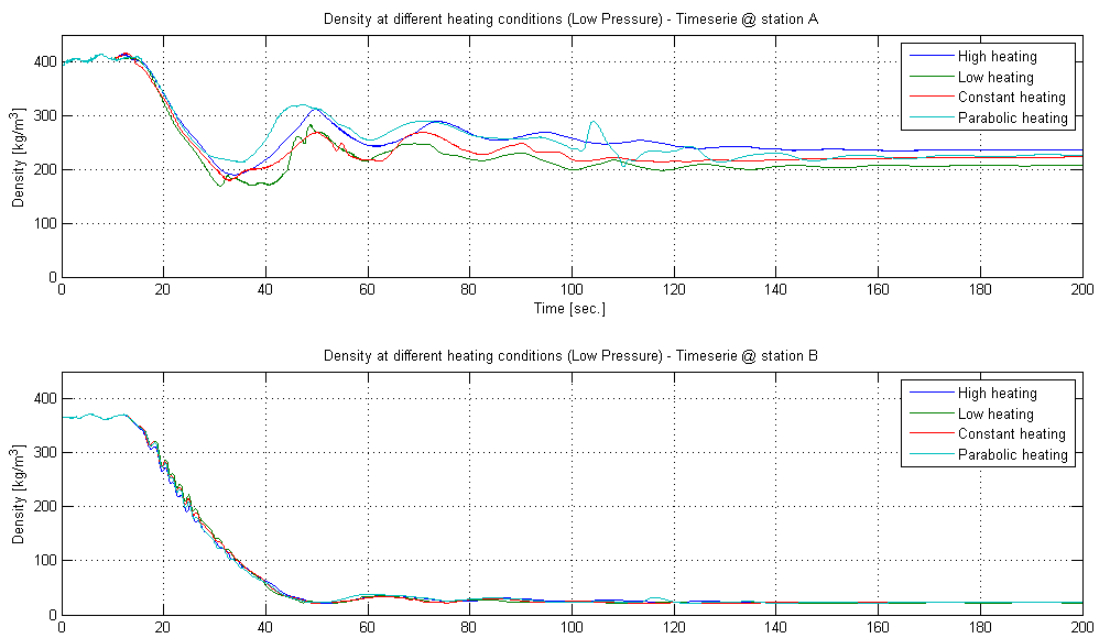


Figure 40: Comparison of the firing profiles on the SKV3 evaporator with respect to fluid density.